Article

Cell Reports

Template-independent genome editing in the *Pcdh15*$^{av-3j}$ mouse, a model of human DFNB23 nonsyndromic deafness

Graphical abstract

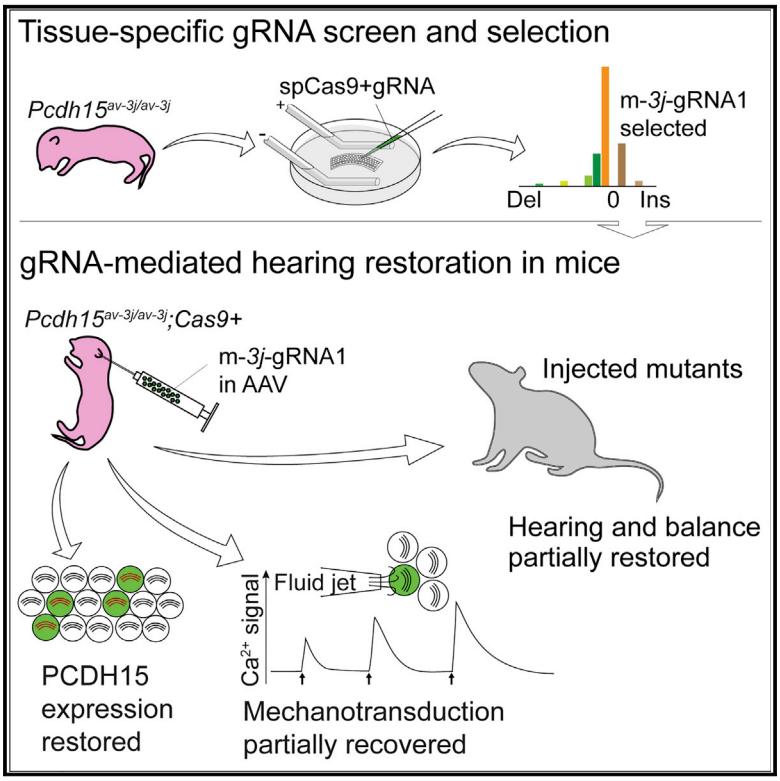

Highlights

- Postmitotic m-*3j*-gRNA1 treatment mediates predominant 1-bp deletion events
- m-*3j*-gRNA1 partially restores frameshift in *Pcdh15*$^{av-3j}$ mutant gene
- m-*3j*-gRNA1 partially restores PCDH15 function in *Pcdh15*$^{av-3j}$ mutant hair cells
- m-*3j*-gRNA1 partially restores hearing and balance of *Pcdh15*$^{av-3j}$ mutant mice

Authors

Lian Liu, Linzhi Zou, Kuan Li, ..., Wenzhi Sun, Qianwen Sun, Wei Xiong

Correspondence

wei_xiong@tsinghua.edu.cn

In brief

Liu et al. use an *ex vivo* cochlea culture system to identify gRNAs that can correct the insertion-induced frameshift mutation in the *av3j* locus. The selected gRNA leads to a partial restoration of hearing and balance functions in *av3j* mutant animals.

Liu et al., 2022, Cell Reports *40*, 111061
July 12, 2022 © 2022 The Author(s).
https://doi.org/10.1016/j.celrep.2022.111061

CellPress

Cell Reports

CellPress
OPEN ACCESS

Article

Template-independent genome editing in the *Pcdh15*$^{av-3j}$ mouse, a model of human DFNB23 nonsyndromic deafness

Lian Liu,[1,2,10] Linzhi Zou,[1,2,10] Kuan Li,[1,3,10] Hanqing Hou,[1,2] Qun Hu,[1,2] Shuang Liu,[1,2] Jie Li,[1,2] Chenmeng Song,[1,2] Jiaofeng Chen,[1,2] Shufeng Wang,[1,2] Yangzhen Wang,[1,2] Changri Li,[4] Haibo Du,[5] Jun-Liszt Li,[6,7] Fangyi Chen,[4] Zhigang Xu,[5] Wenzhi Sun,[6,8] Qianwen Sun,[1,3] and Wei Xiong[1,2,9,11,*]

[1]School of Life Sciences, Tsinghua University, Beijing 100084, China
[2]IDG/McGovern Institute for Brain Research at Tsinghua University, Tsinghua University, Beijing 100084, China
[3]Tsinghua-Peking Joint Center for Life Sciences, Tsinghua University, Beijing 100084, China
[4]Department of Biomedical Engineering, Southern University of Science and Technology, Shenzhen, Guangdong 518055, China
[5]School of Life Sciences, Shandong University, Qingdao, Shandong 266237, China
[6]Chinese Institute for Brain Research, Beijing 102206, China
[7]Academy for Advanced Interdisciplinary Studies (AAIS), Peking University, Beijing 100871, China
[8]School of Basic Medical Sciences, Capital Medical University, Beijing 100069, China
[9]Present address: Chinese Institute for Brain Research, Beijing 102206, China
[10]These authors contributed equally
[11]Lead contact
*Correspondence: wei_xiong@tsinghua.edu.cn
https://doi.org/10.1016/j.celrep.2022.111061

SUMMARY

Although frameshift mutations lead to 22% of inherited Mendelian disorders in humans, there is no efficient *in vivo* gene therapy strategy available to date, particularly in nondividing cells. Here, we show that nonhomologous end-joining (NHEJ)-mediated nonrandom editing profiles compensate the frameshift mutation in the *Pcdh15* gene and restore the lost mechanotransduction function in postmitotic hair cells of *Pcdh15*$^{av-3J}$ mice, an animal model of human nonsyndromic deafness DFNB23. Identified by an *ex vivo* evaluation system in cultured cochlear explants, the selected guide RNA restores reading frame in approximately 50% of indel products and recovers mechanotransduction in more than 70% of targeted hair cells. *In vivo* treatment shows that half of the animals gain improvements in auditory responses, and balance function is restored in the majority of injected mutant mice. These results demonstrate that NHEJ-mediated reading-frame restoration is a simple and efficient strategy in postmitotic systems.

INTRODUCTION

CRISPR-Cas9-based genome-editing techniques provide great opportunities for targeted gene therapy in humans (Cornu et al., 2017; Cox et al., 2015). Unlike gene replacement and gene silencing, genome-editing methods can correct pathogenic mutations with a single treatment, and a subsequent cure may be permanent. Several different genome-editing strategies target distinct types of genetic mutation: homology-dependent strategies can precisely correct mutations according to the sequence of a homologous template (Cox et al., 2015; Suzuki et al., 2019; Yao et al., 2017); homology-independent editing strategies can introduce large insertions within a targeted region, thereby alleviating disorders caused by large deletions (Suzuki et al., 2016); and base-editing techniques can correct substitution mutations (Gaudelli et al., 2017; Koblan et al., 2021; Komor et al., 2016; Nishida et al., 2016; Yeh et al., 2020). Despite these advances, efficient genome-editing strategies that specifically address frameshift mutations in postmitotic cells are lacking.

Newly generated DNA double-strand breaks (DSBs) are repaired mainly through two endogenous DNA repair pathways: precise template-dependent homology-directed repair (HDR) and error-prone template-independent nonhomologous end-joining (NHEJ) pathway (Cox et al., 2015). Although the HDR pathway can theoretically restore scalable mutations based on a donor template, its application is limited due to low recombination efficiency of the HDR pathway and is almost absent in nondividing, terminally differentiated cells/organs (Cox et al., 2015). NHEJ is the major DSB repair mechanism but tends to introduce stochastic insertions/deletions (indels); therefore, it is widely applied in gene disruption. Intriguingly, emerging evidence indicates that CRISPR-Cas9 cleavage-induced indels introduced through NHEJ pathways are nonrandom and mainly guide RNA (gRNA)-sequence-dependent in dividing cells (Allen et al., 2018; Chakrabarti et al., 2019; Koike-Yusa et al., 2014; Leenay et al., 2019; Roman-Rodriguez et al., 2019; Shen et al., 2018; van Overbeek et al., 2016). Further, gRNA-coupled editing profiles in cell lines can be largely predicted using machine learning

This is an open access article under the CC BY-NC-ND license (http://creativecommons.org/licenses/by-nc-nd/4.0/).

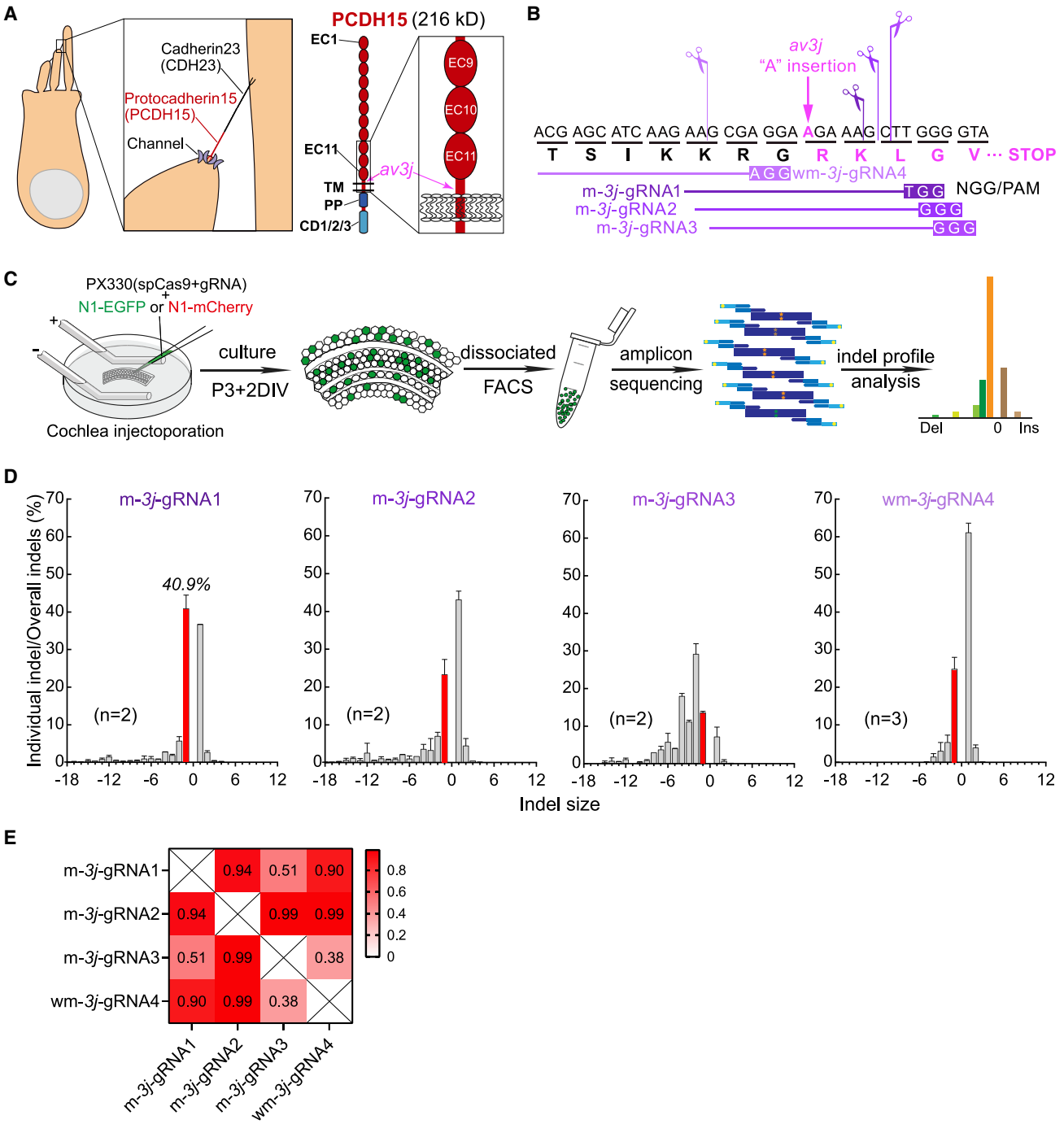

Figure 1. Evaluating indel profiles of gRNAs with *ex vivo* cochlea culture

(A) PCDH15 is one of two tip-link components that gates the mechanotransduction channel in hair cells. The 216-kD PCDH15 contains 11 extracellular cadherin (EC) repeats, a transmembrane (TM) domain, a poly-proline (PP) domain, and a cytoplasmic domain (CD) that includes 3 isoforms. The *av3j* mutation presents an "A" insertion between sequences coding the EC11 and TM domains and causes an early stop codon in the *Pcdh15* gene.

(B) Four 17-nt gRNAs were designed to target the *av3j* "A" insertion site. The m-*3j*-gRNA1, m-*3j*-gRNA2, and m-*3j*-gRNA3 cover the insertion, whereas wm-*3j*-gRNA4 targets both WT and *av3j* alleles (m, mutant; wm, wild-type/mutant).

(C) This illustration depicts the gRNA evaluation procedure in cultured cochlear tissues. P3 cochleae were dissected from the inner ear and injectoporated with a mix of gRNA-carrying PX330 and N1-mCherry or N1-EGFP and then cultured for 2 days *in vitro* (P3 + 2DIV). The injectoporated cells with fluorescence signals were then enriched using FACS. The targeted genome regions were amplified by primers targeting sequences 50–100 bp flanking the gRNA cleavage sites followed by a second PCR to add the Illumina adaptors for deep sequencing. The reads were aligned to correspond wild-type references and quantify the indels of each gRNA.

(legend continued on next page)

models (Allen et al., 2018; Leenay et al., 2019; Shen et al., 2018). However, it remains unclear whether this biased editing exists in nondividing tissue cells and whether it can be used to correct pathogenic frameshift mutations in animals.

In this study, we used an autosomal recessive deafness mouse model of DFNB23—*Pcdh15*$^{av-3J}$ (abbreviated to *av3j* hereafter) (Ahmed et al., 2003), in which a spontaneous insertion of a single adenine (A) nucleobase causes a frameshift in the 7.9 kb *Pcdh15* transcript (Figure 1A), a size that exceeds the maximum payload for the most common delivery vector adeno-associated virus (AAV). The *av3j* mutation causes a truncated PCDH15 protein that lacks the transmembrane and intracellular domains (Alagramam et al., 2001) (Figures 1A and 1B). The 216-kD PCDH15 protein is one of two components that form the tip link to gate the mechanotransduction channel in hair cells (Figure 1A) (Kazmierczak et al., 2007), including the cochlear outer hair cells (OHCs), inner hair cells (IHCs), and vestibular hair cells (VHCs). Hair cells with deficient PCDH15 cannot detect mechanical force, leading to profound congenital deafness and vestibular dysfunction in homozygous *av3j* mice. We explored the possibility of using NHEJ-mediated genome editing to correct a frameshift mutation in the postmitotic hair cells *in vivo* and evaluated restoration effects on hair-cell mechanotransduction, hearing, and balance in *av3j* mutant mice.

RESULTS

Evaluation of gRNA-mediated indel profiles *ex vivo*

By searching the NGG protospacer adjacent motif (PAM) sequence proximal to the inserted "A" within both 15 base-pair (bp) flanks, we designed four gRNAs targeting the *av3j* mutation (m-*3j*-gRNA1, m-*3j*-gRNA2, m-*3j*-gRNA3, and wm-*3j*-gRNA4; m for mutant, w for wild-type, and *3j* for *av3j*) (Figure 1B). The gRNAs with 17 nucleotides were used to obtain greater editing specificity (Fu et al., 2014). To investigate the editing profiles of gRNAs in cochlear hair cells, we established an *ex vivo* gRNA screening system (Figure 1C and STAR Methods) that combined organotypic cochlear culture, injectoporation (Xiong et al., 2014), fluorescence-activated cell sorting (FACS), amplicon sequencing, and editing event profiling. Plasmids containing gRNAs and Cas9 with EGFP or mCherry indicators were injectoporated into the cochleae at postnatal day (P) 3 and further cultured for 2 days *in vitro* (P3 + 2DIV). Because nondividing cells present in the postnatal mouse cochlea (Lee et al., 2006) and injectoporation transfects multiple types of cochlear cells at a limited transfection rate (50–200 cells per cochlea fragment) (Xiong et al., 2014), we obtained postmitotic editing profiles of the target *av3j* site despite cell types. The FACS gate was set relatively low (Figures S1A and S1B) to maximally collect transfected cochlear cells, which show varied fractions of edited reads across replicates and gRNAs (Figure S1C). Compared with the total number of aligned reads, the fraction of edited reads falls within 1%–8% at the FACS-sorted cells (Figure S1D, gray bars) and varies from 13% to 55% (Figure S1E), if corrected simply by counting fluorescence-positive cells (5%–20% in FACS-sorted cells) (Figure S1D, green bars). Among the edited reads, insertion, deletion, and substitution are the main product types (Figure S2A). However, insertions and deletions were only found in treated samples but not in the untransfected control that only contain mistakenly sequenced substitutions, as indicated by percentages in the total aligned reads (Figures S2B and S2C).

Next, we analyzed indel profiles produced by the four gRNAs, presented as the percentage of counted reads for each indel type within the total indel reads at each indel size, ranging from −18 bp to +12 bp (Figure 1D). All four gRNAs showed unique and biased indel profiles that are highly reproducible across replicates (Figure 1D). Among the four gRNAs, m-*3j*-gRNA1, m-*3j*-gRNA2, and wm-*3j*-gRNA4 generated preferred editing at one or two dominant indel sizes (−1 or +1 bp), whereas m-*3j*-gRNA3 introduces countable products over multiple sites (Figure 1D). Importantly, distinct profiles are observed between gRNAs that shift by as little as 1 bp (m-*3j*-gRNA1, m-*3j*-gRNA2, and m-*3j*-gRNA3) (Figures 1B, 1D, and 1E). Considering that the *av3j* mutation is a 1 bp "A" insertion, we propose that 1 bp deletion events can restore the PCDH15 protein back in frame without altering the amino acid number, depicted as red bars in the four gRNA profiles (Figure 1D). As m-*3j*-gRNA1 exhibits the highest percentage (40.9%) of 1 bp deletion, we selected it for function-restoration analysis in subsequent studies.

m-*3j*-gRNA1 restores PCDH15 expression and mechanotransduction

We tested whether m-*3j*-gRNA1-mediated editing restores PCDH15 function in mutant *av3j/av3j* hair cells by injectoporating m-*3j*-gRNA1 and Cas9 into *av3j/av3j* cochleae at P3 + 2DIV (Figure 2A). First, we examined PCDH15 expression in transfected *av3j/av3j* hair-cell bundles, as it is typically absent in *av3j* homozygous mice (Geng et al., 2013). PCDH15 puncta were detected by immunostaining at hair-bundle tips in some injectoporated *av3j/av3j* hair cells but not in surrounding untargeted hair cells and vector-expressed *av3j/av3j* hair cells (Figure 2B). These results show that *ex vivo* gene editing guided by m-*3j*-gRNA1 can mediate effective frame restoration for the *av3j* mutation and recover expression and transportation of PCDH15 proteins to the hair bundle. Next, we applied fluid-jet stimulation and GCaMP6-based Ca^{2+} imaging to assess mechanotransduction of the injectoporated *av3j/av3j* hair cells (Figure 2A). Among the 97 cochlear hair cells we tested, 81 OHCs (Figures 2C–2E) and 16 IHCs (Figure S3), mechanical stimulation responses were restored in 72 (74.2%) hair cells (Figure 2F). This proportion of functionally restored cells was significantly higher than expected, based on 40.9% of 1 bp deletions identified in the editing profile (Figure 1D), suggesting that other frame-restored products may also be functional.

(D) The editing profiles of the 4 gRNAs are identified as the percentage of indel events at each indel size in overall indels. The bars of 1 bp deletion are highlighted in red, which was 40.9% for m-*3j*-gRNA1. Each biological replicate contains two cochleae from one mouse, and the numbers of replicates are shown. Error bars indicate SD.

(E) Pearson correlations of indel spectrum across the 4 gRNAs.

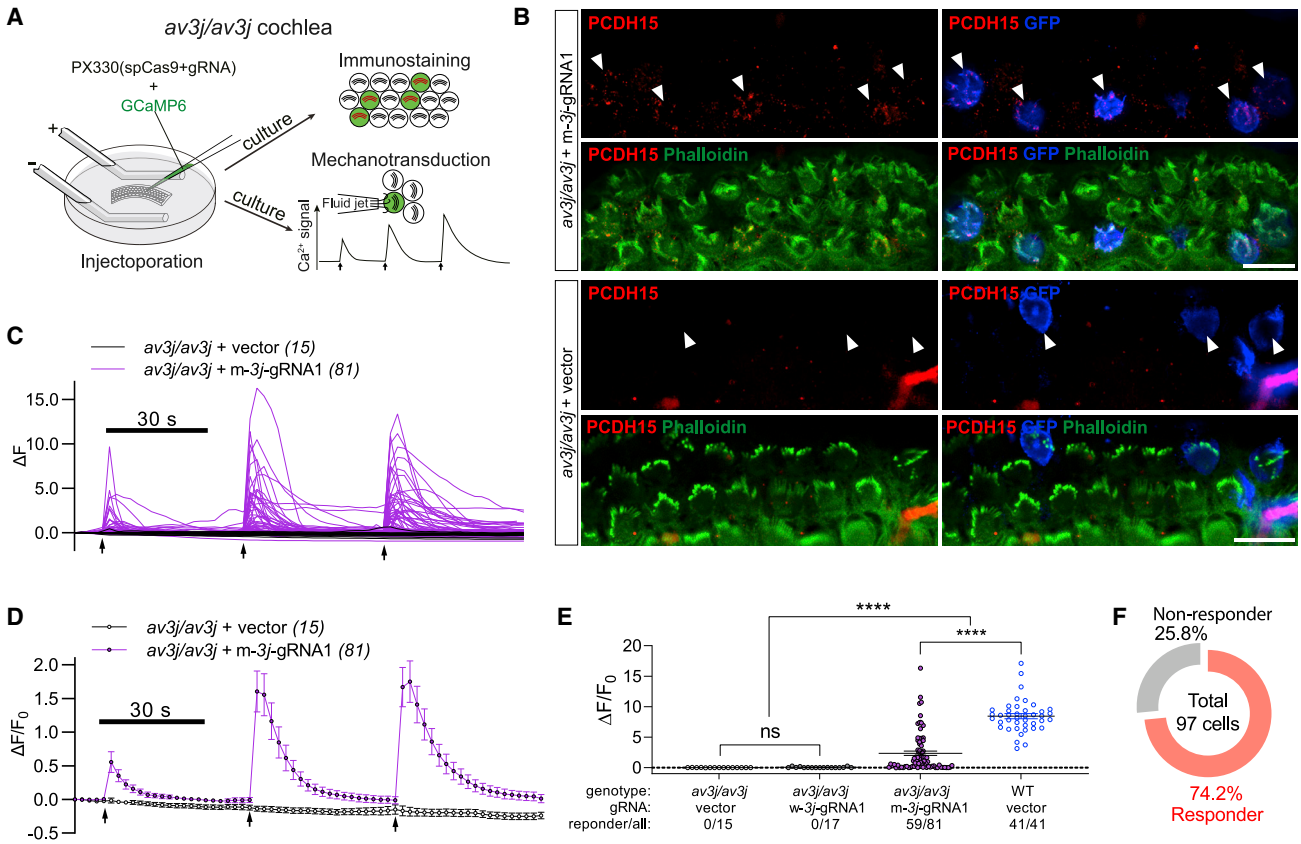

Figure 2. The m-*3j*-gRNA1 restores the *av3j* deficiency *ex vivo*

(A) An illustration depicting procedures following gRNA injectoporation in cultured cochlear tissues.

(B) PCDH15 protein immunostaining in the injectoporated *av3j/av3j* cochleae (P3 + 2DIV). Upper: PX330 containing m-*3j*-gRNA1 and Cas9 (PX330-m-*3j*-gRNA1) was injectoporated together with N1-EGFP. The hair bundles of injectoporated *av3j/av3j* hair cells (indicated by arrowheads) show obvious PCDH15 antibody signals. Lower: empty PX330 and N1-EGFP were expressed. Scale bar, 10 μm.

(C) Traces of Ca^{2+} responses activated by fluid-jet stimuli (black arrow) in *av3j/av3j* OHCs injectoporated by control PX330 vector or PX330-m-*3j*-gRNA1 (P1 + 4 DIV). ΔF is calculated as the absolute change to the Ca^{2+} signal from the first data point (see STAR Methods). The numbers of hair cells is shown.

(D) Averaged traces of Ca^{2+} responses from (C). $\Delta F/F_0$ is calculated as the relative changes in the Ca^{2+} signal from the first data point (see STAR Methods). Error bars indicate SEM.

(E) Quantification of the maximal Ca^{2+} responses in OHCs from recordings similar to (C). W-*3j*-gRNA1 (w for wild-type) targets the corresponding WT sequence and shares the same PAM with m-*3j*-gRNA1. Responsive and total recorded cell numbers are shown. Brown-Forsythe ANOVA tests were applied; ns indicates no significance, ****$p < 0.0001$, error bars indicate SEM.

(F) Following PX330-m-*3j*-gRNA1 transfection, 74.2% (72/97) of *av3j/av3j* auditory hair cells, including both OHCs (D) and IHCs (Figure S3), partially recovered mechanotransduction.

Analysis of frame-restored products of m-*3j*-gRNA1

We investigated the composition and the function of frame-restored editing products of m-*3j*-gRNA1. Statistically, the total frame-restored products (3n-1, n = positive or negative integers) comprised 48.7% of the total indels introduced by m-*3j*-gRNA1 (Figure 3A, black arc). Notably, there are three main-frame-restored types that carry a 1 bp deletion (Del1), a 4 bp deletion (Del4), or a 2 bp insertion (Ins2) and make up 95.1% of total frame-restored indels (Figure 3A, colorful arc). Each type contains one or two top classes of products (Figure 3B). To evaluate mechanotransduction of the three top one products, we synthesized the cDNAs encoding PCDH15-E1373R (Del1-top1), PCDH15-E1373del (Del4-top1), and PCDH15-E1373RK (Ins2-top1) (Figure 3C). As Pcdh15-CD is encoded by at least three isoforms (Figure 1A) and PCDH15-CD2 is known for forming the tip link and the kinociliary link and interacting with TMIE, an integral mechanotransduction channel component (Ahmed et al., 2006; Webb et al., 2011; Zhao et al., 2014), we used PCDH15-CD2 cDNA as the core template. All three constructs recover mechanotransduction of injectoporated *av3j/av3j* hair cells: Del1-top1 and Del4-top1 treatments show Ca^{2+} responses close to the wild-type (WT) PCDH15-CD2 control level, whereas Ins2-top1 yields a lower restoration effect (Figures 3D and 3E). These findings show that at least the three predominant frame-restored products of m-*3j*-gRNA1 can mediate the functional rescue of *av3j/av3j* hair cells, even if the PCDH15 carries 1 or 2 amino acid alterations. These results demonstrate that this frame-restoration

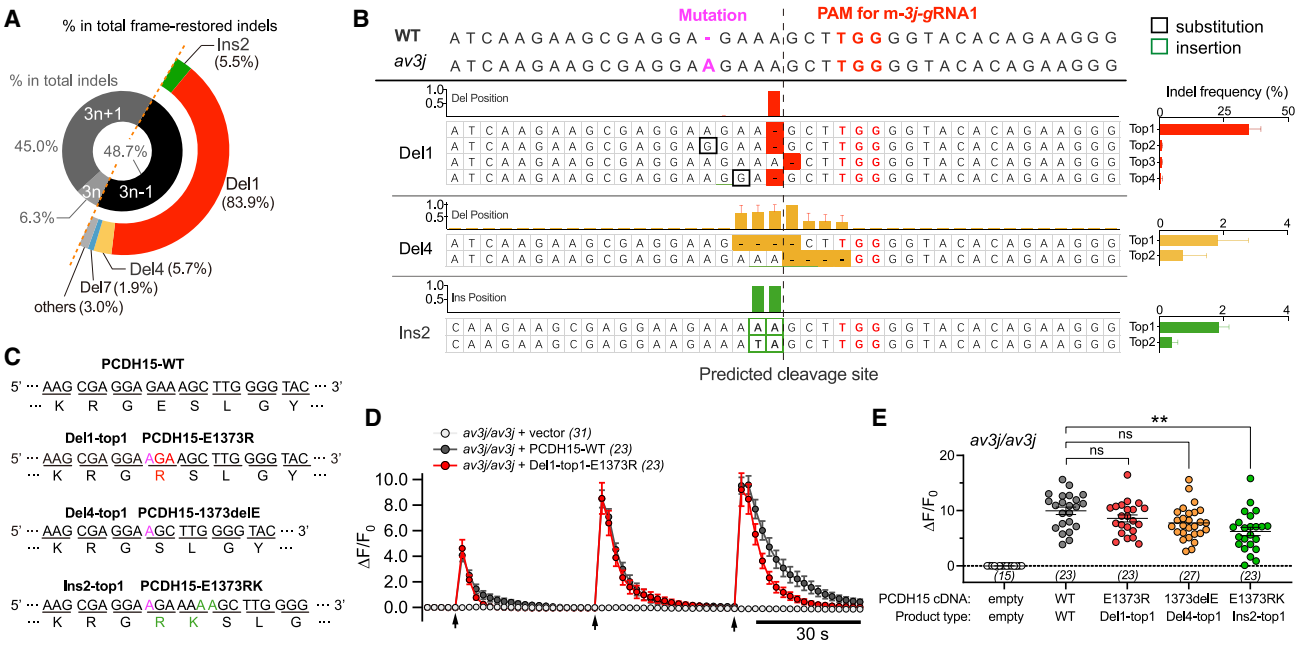

Figure 3. Functional validation of the frame-restored editing products mediated by m-*3j*-gRNA1

(A) In m-*3j*-gRNA1-mediated indels, 48.7% are frame-restored editing products (3n-1), which are dominated by 1 bp deletion (Del1, 83.9%), 4 bp deletion (Del4, 5.7%), and 2 bp insertion (Ins2, 5.5%).

(B) Detailed analysis of frame-restored editing products of m-*3j*-gRNA1, illustrating Del1, Del4, and Ins2 as the most abundant frame-restored types. The histograms on the right indicate the percentage of each editing product in the total indel reads. The *av3j* and WT sequences are shown on top, in which the mutation and PAM sequence are illustrated in magenta and red, respectively. The predicted Cas9 cleavage site is marked using a dashed line at 3 bp upstream from the PAM sequence. These data are drawn from 2 replicates. Error bars indicate SD.

(C) Amino acid changes in the top one frame-restored editing products for each frame-restored type, identified as PCDH15-E1373R (Del1-top1), PCDH15-1373delE (Del4-top1), and PCDH15-E1373RK (Ins2-top1), respectively.

(D) Averaged traces of Ca^{2+} imaging showing the recovery of mechanotransduction in OHCs from cDNA-injectoporated *av3j/av3j* tissues (P2 + 2 DIV). Fluid-jet stimulation time is marked using black arrows. The numbers of hair cells is shown.

(E) Quantification of the maximal elicited Ca^{2+} responses from *av3j/av3j* hair cells injectoporated with plasmid backbone control (empty), PCDH15-WT, PCDH15-E1373R (Del1-top1), PCDH15-1373delE (Del4-top1), and PCDH15-E1373RK (Ins2-top1), respectively. The numbers of hair cells is shown. We applied a Brown-Forsythe ANOVA test; error bars indicate SEM. ns indicates no significance, and $^{**}p < 0.01$.

strategy enables a highly efficient functional restoration of *av3j/av3j* hair cells *ex vivo*.

Comparison of editing profiles between *ex vivo* and *in vivo*

In light of encouraging *ex vivo* observations, we evaluated the restoration potential of m-*3j*-gRNA1 in *av3j* mutant mice (Figure 4A). We packed the m-*3j*-gRNA1 containing U6-gRNA scaffold into the AAV2/9 capsid, with an mCherry expression cassette to indicate virus transfection (AAV-m-*3j*-gRNA1). First, the viral transfection rates of hair cells were counted in WT mice by scala-media injection at P0–P2. The injection offers relatively high efficiency in mice at 14 days postviral delivery (PVD): mCherry occurred in almost 100% of IHCs, and in OHCs and VHCs the transfection rate was approximately 70% and 60%, respectively (Figure S4). Then, we assessed the *in vivo* genome-editing fractions of m-*3j*-gRNA1 in *av3j/av3j* mice with Cas9 knockin background (*av3j/av3j;Cas9*$^{+}$), for which the cochleae and the vestibules were harvested at 2, 4, 8, and 12 weeks PVD (Figure S5). The fractions of editing products are quite stable across replicates as FACS-sorted transfected cells occur in large quantities (Figure S5A); edited reads include percentages between 48% and 75% of total aligned reads (Figure S5B). The overall indel frequency in the aligned reads increases progressively and reaches a plateau as early as 4 weeks of age, which are ~57% in cochlear tissues and ~70% in vestibular organs (Figure 4B). There are few substitutions (<0.8%) in overall aligned reads (Figure S5C, mustard bars), and indels are the major contributor (>95%) in edited reads (Figure S5C, purple bars).

We carried out a detailed analysis of the *in vivo* data from 4-week cochlea and vestibule samples and the *ex vivo* data from injectoporated cochleae. While comparing their indel profiles, Del1 and Ins1 are again predominant in the cochleae and vestibules (containing all 3 cristae) both *in vivo* and *ex vivo*, where the −1 bp deletion events reach 19.2% of the total aligned reads (Figure 4C). Importantly, the overall frame-restored products occupy more than 40% of the indels from cochlea *ex vivo* and *in vivo* (Figure 4D), and the proportions of the top three function-restored products dominate all frame-restored indels (Figure 4E). Nevertheless, the predominant frame-restored products displayed identical indel

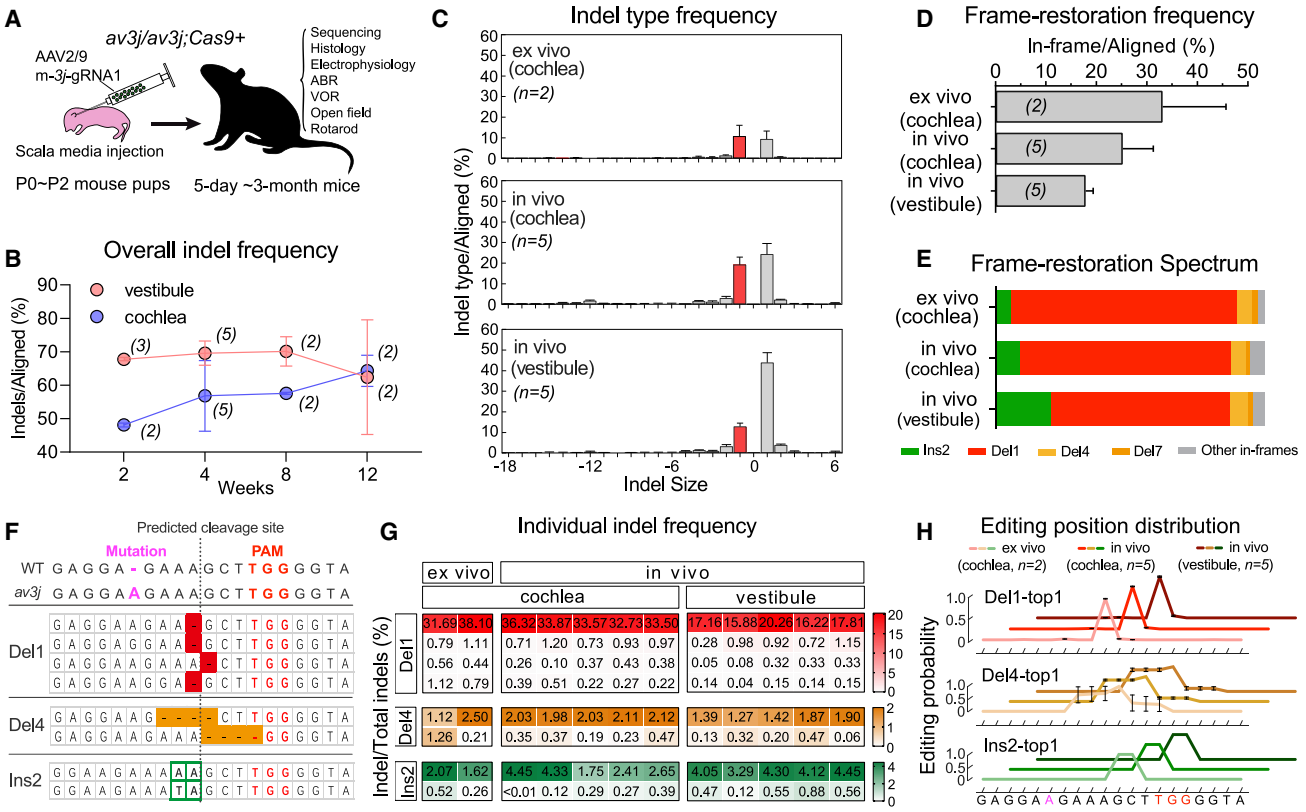

Figure 4. Similar editing profiles of m-*3j*-gRNA1 between *ex vivo* and *in vivo*

(A) An illustration depicting the overall *in vivo* gene delivery and evaluation procedures. AAV2/9-U6-m-*3j*-gRNA1-CMV-mCherry (abbreviated as AAV-m-*3j*-gRNA1) was injected into the scala media of P0–P2 *av3j/av3j;Cas9*$^{+}$ mice bilaterally, followed by a variety of measurements over time.

(B) Percentages of the total indels in virus transfected cells of cochleae and vestibules over time. The tissues were harvested in the injected mice at 2, 4, 8, and 12 weeks postviral delivery (PVD). The transfected cells were enriched by FACS based on mCherry fluorescence and extracted for sequencing, followed by an editing profile analysis.

(C) The editing profiles of PX330-m-*3j*-gRNA1 injectoporated cochlear cultures (cochlea *ex vivo*, P3 + 2DIV), AAV-m-*3j*-gRNA1 transfected cochleae (cochlea *in vivo*, 4 weeks PVD), and AAV-m-*3j*-gRNA1 transfected vestibules (vestibule *in vivo*, 4 weeks PVD). Top: note that displayed *ex vivo* data originated from Figure 1D and are corrected with aligned reads in this figure.

(D) Frame-restoration frequency showing percentages of frame-restored editing products in the total indel products.

(E) Frame-restoration spectrum showing percentages of each in-frame product in the total in-frame editing products.

(F) Mutant and WT sequences are presented. In the top three types of frame-restored products, Del1, Del4, and Ins2, each type contains between two and four individual products. The *av3j* mutation and PAM sequence are illustrated in magenta and red. The predicted Cas9 cleavage site is indicated using a dashed line at 3bp upstream of the NGG PAM.

(G) The percentage of each individual editing product across all indels, with each column indicating a single replicate. Each type of indel product with the same indel size is dominated by one (rarely two) individual editing product.

(H) The indel position analysis shows normalized editing frequency at each nucleotide, suggesting the same high-frequency individual editing products across conditions. Color intensity: lightest, cochlea *ex vivo*; medium, cochlea *in vivo*; darkest: vestibule *in vivo*. In (B), (C), (D), (G), and (H), each biological replicate contains two cochleae from one mouse for *ex vivo* data and two organs from one mouse for *in vivo* data. The numbers of replicates are shown. Error bars indicate SD.

positions and inserted bases (Figures 4F–4H). The frame-restoration frequency and indel percentiles are more similar within cochlear samples (*in vivo* and *ex vivo*) compared with those from vestibular organs (*in vivo*), indicating a tissue-specific bias in NHEJ-mediated genome editing (Figures 4C–4E). Small indel products may be further cut to produce larger deletions in long-time genome editing (van Overbeek et al., 2016); therefore, we analyzed the editing profiles of AAV-delivered m-*3j*-gRNA1 in the cochleae and vestibules at 2, 4, 8, and 12 weeks PVD and found they were stable at all time points (Figures S6). We also analyzed potential off-target effects for long-term AAV-mediated expression (Figure S7). Based on inner ears collected from injected *av3j/av3j;Cas9*$^{+}$ animals at 4, 8, 12, and 16 weeks PVD, we tested the top 16 off-target sites predicted by CCTop and Cas-OFFinder using amplicon sequencing (see STAR Methods). Among these sites, 2 of 16 selected off-target sites showed detectable editing, with average indel frequencies of 0.7% and 0.3% (Figure S7). These data demonstrate that *ex vivo* screening and evaluation facilitate the assessment of genome-editing outcomes and performance of target gRNAs before applying the frame-restoration strategy *in vivo*.

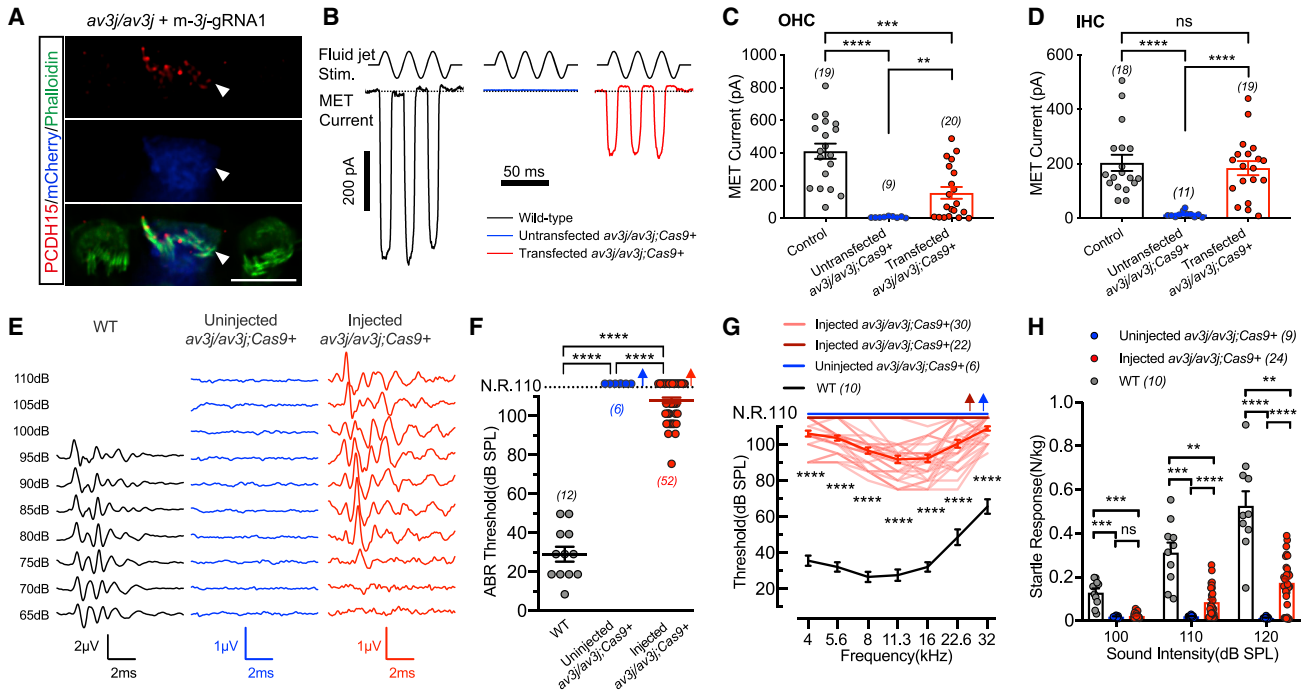

Figure 5. *In vivo* delivery of m-*3j*-gRNA1 ameliorates auditory function of *av3j/av3j;Cas9*$^+$ mice

(A) PCDH15 immunostaining (red) shows the recovery of protein expression in the stereocilium tips in transfected OHCs (blue) from AAV-injected *av3j/av3j;Cas9*$^+$ mice (tissue harvested 5 days PVD). The hair bundle was stained with phalloidin (green). Scale bar, 6 μm.

(B) Representative examples of mechanotransduction (MET) currents recorded from OHCs in control and *av3j/av3j;Cas9*$^+$ mice with or without transfection (10 days PVD). A fluid jet was used to stimulate the hair bundle during recordings.

(C and D) Quantification of the MET current amplitudes from recordings similar to (B) in OHCs (C) and IHCs (D). In injected *av3j/av3j;Cas9*$^+$ mice, 14 of 20 OHCs and 18 of 19 IHCs were responsive. Littermate *av3j/*$^+$*;Cas9*$^+$ or WT mice and uninjected *av3j/av3j;Cas9*$^+$ mice at the same age were used as controls.

(E) Representative click ABR waveforms from 4 to 5 weeks WT, uninjected, and injected *av3j/av3j;Cas9*$^+$ mice.

(F) Mean click ABR thresholds in WT (gray), uninjected (blue), and injected (red) *av3j/av3j;Cas9*$^+$ mice. Arrows indicate instances of no responses even at the maximal stimulus level (110 dB SPL). This is also illustrated using the dashed line labeled with N.R.110 (nonresponsive at 110 dB SPL).

(G) Mean pure-tone ABR thresholds in WT (black), uninjected (blue), and injected (red, individual pure-tone ABR thresholds of responsive animals shown in light red, nonresponsive animals in dark red) *av3j/av3j;Cas9*$^+$ mice. In (F) and (G), 30 of 52 injected *av3j/av3j;Cas9*$^+$ mice recovered ABR responses.

(H) Acoustic startle responses to white noise were recorded in 4–6 week WT (gray), uninjected (blue), and injected (red) *av3j/av3j;Cas9*$^+$ mice; 24 injected mice with detectable ABR were used in the startle response test. In (C) and (D), each cell was counted as a replicate. In (F), (G), and (H), each animal was counted as a replicate. The numbers of animals is shown. A Brown-Forsythe and Welch ANOVA test was used. Error bars indicate SEM. ns indicates no significance, *$p < 0.05$, **$p < 0.051$, ***$p < 0.001$, and ****$p < 0.0001$.

Characterization of hearing function in injected *av3j* mutant mice

We examined PCDH15 protein expression and localization in AAV-m-*3j*-gRNA1-injected *av3j/av3j;Cas9*$^+$ mice. The PCDH15 protein expression was recovered after treatment, as PCDH15 puncta were observed in the hair bundle of the transfected *av3j/av3j;Cas9*$^+$ OHCs at 5 days PVD (Figure 5A). To investigate the recovery of mechanotransduction after m-*3j*-gRNA1 treatment, we measured the fluid-jet evoked mechanotransduction currents by whole-cell patch-clamp recording in OHCs and IHCs of injected *av3j/av3j;Cas9*$^+$ mice and control mice at 10 days PVD (Figures 5B–5D). As hair cell rescue is associated with a variety of edited PCDH15 proteins that may differentially impact mechanotransduction kinetics, we counted the number of rescued hair cells using a fluid jet at moderate intensity to avoid physical damage to the hair bundle. Mechanotransduction currents were restored at various amplitudes in 14 of 20 (70%) transfected OHCs and in 18 of 19 (94.7%) transfected IHCs (Figures 5C and 5D), which is consistent with the high proportion of functional restoration observed *ex vivo* (Figure 2E). To calculate the gross percentage of targeted auditory hair cells with functional restoration *in vivo*, we used a dye indicator of mechanotransduction channel opening, styryl FM 5-95 (Meyers et al., 2003), to treat the cochlea of injected *av3j/av3j;Cas9*$^+$ mice at 7–10 days PVD. Among 929 transfected OHCs identified by mCherry fluorescence, 78.3% of these OHCs exhibited an uptake of FM 5-95 dye (Figure S8). Similarly, uptake ratios were 84.7% in IHCs and 84.4% in VHCs (Figure S8).

We recorded auditory brainstem responses (ABRs) in injected *av3j/av3j;Cas9*$^+$ mice at 4–5 weeks PVD to evaluate hearing restoration. We found that 30 of the 52 injected mice showed ABRs; however, no responses were observed in uninjected *av3j/av3j;Cas9*$^+$ animals (Figures 5E–5G). The remaining 22 injected mice were not rescued, likely due to low virus transfection rates or injection failure. The best-performing mice showed visible click ABR thresholds at 75 dB sound pressure level

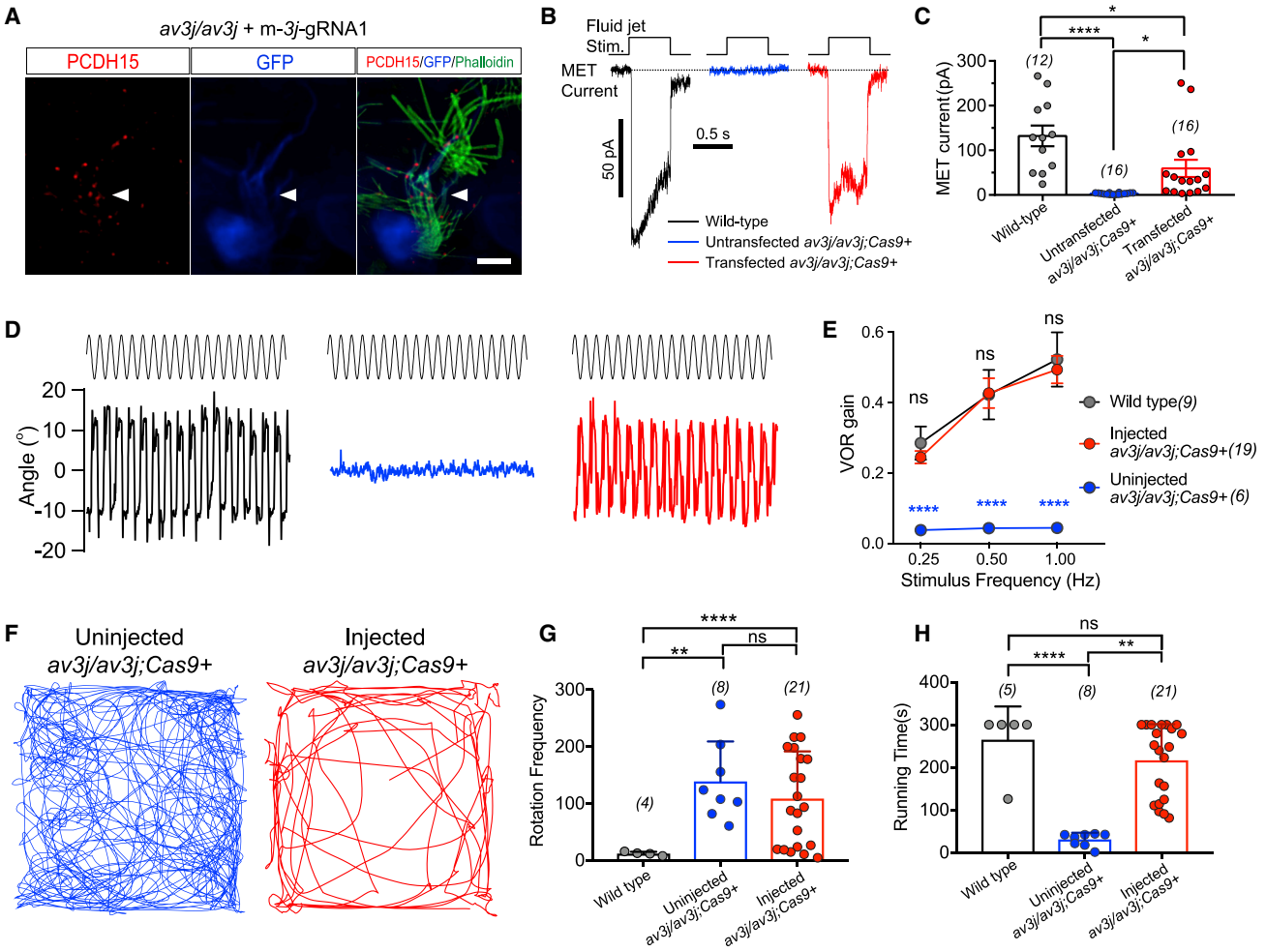

Figure 6. *In vivo* delivery of m-*3j*-gRNA1 ameliorates vestibular symptom of *av3j/av3j;Cas9*$^+$ mice

(A) PCDH15 protein expression (red) was recovered in the stereocilium tips of transfected vestibular hair cells (VHCs, blue) from injected *av3j/av3j;Cas9*$^+$ mice (10 days PVD). The hair bundle was stained with phalloidin (green). Note that only the hair bundles of transfected *av3j/av3j* hair cells showed obvious signals (marked by an arrowhead). Scale bar, 3 μm.

(B) Representative examples of mechanotransduction currents recorded from VHCs in WT, uninjected, and injected *av3j/av3j;Cas9*$^+$ mice (10 days PVD). A fluid jet was used for stimulation.

(C) Quantification of the mechanotransduction current amplitudes from recordings similar to (B). For transfected *av3j/av3j;Cas9*$^+$ VHCs, 10 of 16 (62.5%) were responsive. P10 WT mice were used as positive control. Cell numbers are shown.

(D) Representative traces of VOR responses from WT, uninjected, and injected *av3j/av3j;Cas9*$^+$ mice.

(E) Quantification of the VOR gain. The responses of injected animals (red) show no differences from WT mice (gray) across all frequencies, compared with a lack of responses in uninjected *av3j/av3j;Cas9*$^+$ mice (blue).

(F) Examples of open-field locomotion traces of uninjected *av3j/av3j;Cas9*$^+$ littermates (blue) and injected *av3j/av3j;Cas9*$^+$ mice (red).

(G) Comparisons across circling frequencies during open-field tests.

(H) Comparisons across running times in the rotarod test obtained in WT, uninjected, and injected *av3j/av3j;Cas9*$^+$ mice. In (C), each cell was counted as a replicate. In (E), (G), and (H), each animal was counted as a replicate. The numbers of animals is shown. A Brown-Forsythe and Welch ANOVA test was used. ns indicates no significance, **p < 0.05, **p < 0.01, and ****p < 0.0001; error bars indicate SEM.

(SPL) (Figures 5E and 5F). Compared with the uninjected mutants, significantly lower tone ABR thresholds were observed in the injected *av3j/av3j;Cas9*$^+$ mice at all tested frequencies, with the greatest improvement at 11.3 and 16 kHz (Figure 5G), in which 7 mice exhibited ABR thresholds equal or less than 80 dB SPL (11.3 kHz, 4 mice exhibited ABR at 75 dB SPL, 3 at 80 dB SPL, and 16 kHz, 3 mice at 75 dB SPL, 4 at 80 dB SPL; see Table S1). To evaluate the recovery of hearing-associated behavior in injected mice, acoustic startle responses were tested by using random white noise stimulation at multiple sound intensities (100–120 dB SPL) in mice with detectable ABRs. Among 24 mice tested, 22 animals showed recovered acoustic startle responses, and the averaged amplitude at 120 dB SPL was ~40% of that of the control WT mice (Figure 5H and Table S1).

We noted that auditory function restoration in adult DFNB23 mice remains limited. As gradual hair-cell loss occurs in *av3j* homozygous mice (Pawlowski et al., 2006), we quantified hair-cell survival in mice at 2 months PVD to evaluate whether our treatment alleviates this pattern in adult mice. Following treatment, hair-cell survival improved in the apical turn, whereas cell death in the middle and basal turns was not significantly reversed, and OHCs were more severely lost than IHCs (Figure S9).

Analysis of vestibular function in injected *av3j* mice

In addition to profound deafness, *av3j* mice also demonstrate severe balance challenges due to a lack of mechanotransduction in VHCs. As such, we evaluated the vestibular function of injected *av3j/av3j;Cas9*$^+$ mice. At 10 days PVD, PCDH15 protein expression was detected in transfected VHCs (Figure 6A). In 16 transfected VHCs, 10 (62.5%) restored mechanotransduction currents (Figures 6B and 6C). To assess the overall vestibular function in injected mice, we recorded the vestibulo-ocular reflex (VOR), a physiological response that allows the vestibular system to detect head motion and triggers movement in the opposite eye to stabilize vision. The injected *av3j/av3j;Cas9*$^+$ mice recovered VOR at close to WT levels at all tested rotation frequencies, in contrast to uninjected *av3j/av3j;Cas9*$^+$ mice whose VOR was totally absent (Figures 6D and 6E). Then, we performed open-field and rotarod tests to further examine restoration of balance. In the open-field test, circling frequencies were diminished in injected *av3j/av3j;Cas9*$^+$ mice, where 7 of 21 injected animals nearly stopped all circling behavior (Figures 6F and 6G). In the rotarod test, all injected *av3j/av3j;Cas9*$^+$ animals ran on the rotating rod for longer durations than did uninjected *av3j/av3j;Cas9*$^+$ animals (Figure 6H). Six injected *av3j/av3j;Cas9*$^+$ mice remained standing on the rod once the test was complete (after 300s), similar to the best-performing WT animals, indicating an nearly full recovery to balance.

DISCUSSION

Here, we present that the *in vivo* frame-restoration strategy, which is based on the gRNA-Cas9-induced precise cleavage and the NHEJ-mediated highly biased editing, can correct frameshift mutations in the postmitotic cells of an organ with unprecedented effectiveness and efficiency. We believe that this NHEJ-mediated frame-restoration strategy holds great promise for developing treatments for small indel-induced frameshift mutations, thereby presenting new intervention opportunities across 22% of inherited Mendelian disorders in humans (Stenson et al., 2003).

Characteristics of the frame-restoration strategy

In the *av3j* mouse model of DFNB23, the high degree of mechanotransduction recovery in hair cells (OHC 78.3%; IHC 84.7%; and VHC 84.4%), as evaluated by FM dye uptake (Figure S8), alleviates symptoms in disrupted hearing and balance. Because NHEJ is the major DSB repair pathway in most cell types, including in both dividing and nondividing cells (Symington and Gautier, 2011), this frame-restoration strategy is theoretically applicable to any organs. Moreover, unlike homology-dependent editing strategies, NHEJ does not require template DNA, largely simplifying probe design and delivery. gRNA selection is highly flexible when applying this frame-restoration strategy. We demonstrate that gRNAs shift in only 1 bp (e.g., m-*3j*-gRNA1, m-*3j*-gRNA2, and m-*3j*-gRNA3) and exhibit entirely different editing profiles with distinct indel dominance (Figures 1B and 1D), providing a variety of restoration options. The NHEJ-mediated 1 bp insertion and 1 bp deletion are the predominant elements in most editing profiles and compensate the frameshift mutation in the target site while leaving small-scale amino acid alterations in translated protein products. Our data reveal that, for less conserved regions, an imperfect correction with small amino acid alterations can still significantly restore functional phenotypes (Figure 3), and this largely extends the range for gRNA selection.

Application of the frame-restoration strategy in inherited deafness

Gene therapy interventions for congenital deafness have advanced considerably in the last decade. Gene replacement is the most common and successful genetic manipulation in this area (Akil et al., 2012, 2019; Emptoz et al., 2017; Nist-Lund et al., 2019; Pan et al., 2017; Yu et al., 2014), although it is limited by the loading capacity of delivery vectors (e.g., 4.7 kb for AAV), rendering gene therapy for large proteins nearly impossible. Recent progress in genome-editing-based *in vivo* deafness gene therapy shows significant hearing improvements in models with postnatal progressive hearing loss that harbor missense mutations on *Tmc1* (cDNA 2.3 kb), using either reading-frame disruption of dominant-negative allele (Gao et al., 2018; Gyorgy et al., 2019) or base editing (Yeh et al., 2020). Here, we demonstrate that, in the DFNB23 animal model exhibiting profound congenital deafness, the frame-restoration strategy recovers 7.9 kb *Pcdh15* gene function and mitigates hearing and balance symptoms.

Fraction of the function-restored hair cells in injected *av3j* mice

PCDH15 is well known for its role in forming the tip link (Figure 1A); therefore, edited PCDH15 in *av3j* mice with restored hair-bundle localization and mechanotransduction may recover hair-cell function and hearing function. Because the *av3j* mutation is recessive, frame restoration of one *Pcdh15* allele in an *av3j* mutant hair cell is sufficient for functional restoration. Assuming that frame-restored indel events are completely random in either allele of transfected cells and considering the *in vivo* cochlea data (Figure 4D), the frame-restoration frequency of 25.2% likely reaches a proportion of corrected hair cells at $2 \cdot 0.252 - 0.252^2$ that equals 44%. This is substantially lower than the observed ratios of functionally rescued OHCs (78.3%) and IHCs (84.7%) (Figure S8). One possible explanation is that mutant hair cells without functional rescue were dying and therefore were not counted. As viral transfection was observed in almost 70% OHCs and 100% IHCs (Figure S4), an estimated ~30.8% of OHCs and ~44% of IHCs are rescued in optimal conditions. In AAV-injected *av3j* mice, unrecovered and disorganized hair bundles were observed in transfected hair cells along the entire cochleae (Figure 5A), which may account for the smaller amplitude of mechanotransduction currents in targeted

hair cells (Figures 5B–5D) and the decreased wave I in ABR waveforms (Figure 5E). These data further indicate that PCDH15 is relevant not only for mechanotransduction but also for the development and organization of hair bundles as well as for hair-cell maintenance and survival, which is consistent with our observation that most of the OHCs were lost in adult *av3j/av3j;Cas9*$^{+}$ animals (Figure S9). Conversely, vestibular function was recovered to a greater extent, despite VHCs transfected at a ratio of 60% (similar to OHCs at 70%). We speculate that VHCs require fewer precise functions related to PCDH15-dependent tip-link formation and hair-bundle maturation. Considering that the PCDH15 begins its expression in the cochlear epithelium as early as embryonic day 12 (Murcia and Woychik, 2001), further study is needed to identify the optimal time window for *Pcdh15* gene.

Limitations of the study

We demonstrate a proof-of-concept case of *in vivo* gene correction for frameshift mutation in the auditory epithelium, which, however, was from the *av3j* mouse line with *Cas9* transgene background. Because exogenous Cas9 delivery achieves significantly less expression level, our study does not represent a real translational scenario. With further AAV-deliverable Cas9 optimization, such as highly efficient dual AAVs, the frame-restoration strategy will be better positioned for clinical applications.

With limited choices of PAM, the frame-restored products always carry amino acid insertion or deletion. Combining with new editing tools (e.g., PAMless CRISPR-Cas9 variants [Walton et al., 2020] enabling a more flexible gRNA design) will allow more precise frameshift correction in a wide range of pathogenic sites.

STAR★METHODS

Detailed methods are provided in the online version of this paper and include the following:

- KEY RESOURCES TABLE
- RESOURCE AVAILABILITY
  - Lead contact
  - Materials availability
  - Data and code availability
- EXPERIMENTAL MODEL AND SUBJECT DETAILS
- METHOD DETAILS
  - Design of gRNAs and plasmid construction
  - Cochlear tissue culture and injectoporation
  - Tissue digestion and FACS
  - DNA sequencing library construction
  - Immunofluorescence
  - Cochlea calcium imaging
  - Virus injection
  - Off-target prediction
  - Whole-cell electrophysiology of hair cells
  - FM5-95 loading and imaging
  - Auditory brainstem response (ABR)
  - Acoustic startle response
  - Vestibulo-ocular reflex (VOR)
  - Open field test
  - Rotarod test
- QUANTIFICATION AND STATISTICAL ANALYSIS
  - Bioinformatic analysis
  - Ca^{2+} imaging data analysis
  - VOR analysis
  - Statistical analysis

SUPPLEMENTAL INFORMATION

Supplemental information can be found online at https://doi.org/10.1016/j.celrep.2022.111061.

ACKNOWLEDGMENTS

We thank Yanhui Chen and Dr. Bai Lu for providing the equipment to measure the acoustic startle response and rotarod. Thanks to Chris Walters of Tucker-Davis Technologies for technical help with ABR recordings, to Drs. Chunlai Chen, Yinqing Li, Xin Liang, and members of Xiong laboratory for helpful discussions, and to Life Science Editors for their professional editing services. We also thank the Imaging Core Facility, Technology Center for Protein Sciences at Tsinghua University, for assistance with using imaging instruments and software and the Tsinghua University Branch of China National Center for Protein Sciences (Beijing) and Tsinghua University Technology Center for Protein Research for the cell function analyzing facility support. We extend thanks to the Core Facility of the Center of Biomedical Analysis, Tsinghua University, for assistance with L780 confocal microscopy. This work was supported through the National Natural Science Foundation of China (31522025, 31571080, 81873703, and 31861163003, to W.X.), China Ministry of Science and Technology (2021ZD0203304, to W.X.), and a startup fund from the Tsinghua-Peking Center for Life Sciences. W.X. is a CIBR cooperative investigator (2020-NKX-XM-04), funded by the Open Collaborative Research Program of Chinese Institute for Brain Research.

AUTHOR CONTRIBUTIONS

L.L. completed gRNA design, construction, FACS and deep sequencing, tissue culture and injectoporation, mouse surgery and viral injection, and behavioral testing; L.Z. performed the cochlear culture and injectoporation, immunostaining, and plasmid preparation; K.L. performed genome data mining; H.H. carried out behavioral test and immunostaining data quantification; Q.H. performed the cochlear culture and injectoporation; S.L. completed the hair-cell electrophysiology and behavioral data analysis; J.L., C.S., J.C., S.W., Y.W., C.L., H.D., and J.-L.L. conducted the experiments; F.C., Z.X., W.S., and Q.S. supervised some of the experiments; and L.L. and W.X. designed the experiments, generated the figures, and wrote the manuscript.

DECLARATION OF INTERESTS

The authors declare no competing interest.

Received: June 20, 2021
Revised: April 15, 2022
Accepted: June 14, 2022
Published: July 12, 2022

REFERENCES

Ahmed, Z.M., Goodyear, R., Riazuddin, S., Lagziel, A., Legan, P.K., Behra, M., Burgess, S.M., Lilley, K.S., Wilcox, E.R., Riazuddin, S., et al. (2006). The tip-link antigen, a protein associated with the transduction complex of sensory hair cells, is protocadherin-15. J. Neurosci. *26*, 7022–7034. https://doi.org/10.1523/JNEUROSCI.1163-06.2006.

Ahmed, Z.M., Riazuddin, S., Ahmad, J., Bernstein, S.L., Guo, Y., Sabar, M.F., Sieving, P., Riazuddin, S., Griffith, A.J., Friedman, T.B., et al. (2003). PCDH15 is expressed in the neurosensory epithelium of the eye and ear and mutant alleles

are responsible for both USH1F and DFNB23. Hum. Mol. Genet. *12*, 3215–3223. https://doi.org/10.1093/hmg/ddg358.

Akil, O., Dyka, F., Calvet, C., Emptoz, A., Lahlou, G., Nouaille, S., Boutet de Monvel, J., Hardelin, J.P., Hauswirth, W.W., Avan, P., et al. (2019). Dual AAV-mediated gene therapy restores hearing in a DFNB9 mouse model. Proc. Natl. Acad. Sci. USA *116*, 4496–4501. https://doi.org/10.1073/pnas.1817537116.

Akil, O., Seal, R.P., Burke, K., Wang, C.S., Alemi, A., During, M., Edwards, R.H., and Lustig, L.R. (2012). Restoration of hearing in the VGLUT3 knockout mouse using virally mediated gene therapy. Neuron *75*, 283–293. https://doi.org/10.1016/j.neuron.2012.05.019.

Alagramam, K.N., Murcia, C.L., Kwon, H.Y., Pawlowski, K.S., Wright, C.G., and Woychik, R.P. (2001). The mouse Ames waltzer hearing-loss mutant is caused by mutation of Pcdh15, a novel protocadherin gene. Nat. Genet. *27*, 99–102. https://doi.org/10.1038/83837.

Allen, F., Crepaldi, L., Alsinet, C., Strong, A.J., Kleshchevnikov, V., De Angeli, P., Páleníková, P., Khodak, A., Kiselev, V., Kosicki, M., et al. (2018). Predicting the mutations generated by repair of Cas9-induced double-strand breaks. Nat. Biotechnol. *37*, 64–72. https://doi.org/10.1038/nbt.4317.

Bae, S., Park, J., and Kim, J.S. (2014). Cas-OFFinder: a fast and versatile algorithm that searches for potential off-target sites of Cas9 RNA-guided endonucleases. Bioinformatics *30*, 1473–1475. https://doi.org/10.1093/bioinformatics/btu048.

Chakrabarti, A.M., Henser-Brownhill, T., Monserrat, J., Poetsch, A.R., Luscombe, N.M., and Scaffidi, P. (2019). Target-specific precision of CRISPR-mediated genome editing. Mol. Cell *73*, 699–713.e6. https://doi.org/10.1016/j.molcel.2018.11.031.

Clement, K., Rees, H., Canver, M.C., Gehrke, J.M., Farouni, R., Hsu, J.Y., Cole, M.A., Liu, D.R., Joung, J.K., Bauer, D.E., and Pinello, L. (2019). CRISPResso2 provides accurate and rapid genome editing sequence analysis. Nat. Biotechnol. *37*, 224–226. https://doi.org/10.1038/s41587-019-0032-3.

Cornu, T.I., Mussolino, C., and Cathomen, T. (2017). Refining strategies to translate genome editing to the clinic. Nat. Med. *23*, 415–423. https://doi.org/10.1038/nm.4313.

Cox, D.B.T., Platt, R.J., and Zhang, F. (2015). Therapeutic genome editing: prospects and challenges. Nat. Med. *21*, 121–131. https://doi.org/10.1038/nm.3793.

Edelstein, A., Amodaj, N., Hoover, K., Vale, R., and Stuurman, N. (2010). Computer control of microscopes using microManager. Curr. Protoc. Mol. Biol. Chapter 14, Unit14.20. https://doi.org/10.1002/0471142727.mb1420s92.

Emptoz, A., Michel, V., Lelli, A., Akil, O., Boutet de Monvel, J., Lahlou, G., Meyer, A., Dupont, T., Nouaille, S., Ey, E., et al. (2017). Local gene therapy durably restores vestibular function in a mouse model of Usher syndrome type 1G. Proc. Natl. Acad. Sci. USA *114*, 9695–9700. https://doi.org/10.1073/pnas.1708894114.

Fu, Y., Sander, J.D., Reyon, D., Cascio, V.M., and Joung, J.K. (2014). Improving CRISPR-Cas nuclease specificity using truncated guide RNAs. Nat. Biotechnol. *32*, 279–284. https://doi.org/10.1038/nbt.2808.

Gao, X., Tao, Y., Lamas, V., Huang, M., Yeh, W.H., Pan, B., Hu, Y.J., Hu, J.H., Thompson, D.B., Shu, Y., et al. (2018). Treatment of autosomal dominant hearing loss by in vivo delivery of genome editing agents. Nature *553*, 217–221. https://doi.org/10.1038/nature25164.

Gaudelli, N.M., Komor, A.C., Rees, H.A., Packer, M.S., Badran, A.H., Bryson, D.I., and Liu, D.R. (2017). Programmable base editing of A*T to G*C in genomic DNA without DNA cleavage. Nature *551*, 464–471. https://doi.org/10.1038/nature24644.

Geng, R., Sotomayor, M., Kinder, K.J., Gopal, S.R., Gerka-Stuyt, J., Chen, D.H.C., Hardisty-Hughes, R.E., Ball, G., Parker, A., Gaudet, R., et al. (2013). Noddy, a mouse harboring a missense mutation in protocadherin-15, reveals the impact of disrupting a critical interaction site between tip-link cadherins in inner ear hair cells. J. Neurosci. *33*, 4395–4404. https://doi.org/10.1523/JNEUROSCI.4514-12.2013.

Gyorgy, B., Nist-Lund, C., Pan, B., Asai, Y., Karavitaki, K.D., Kleinstiver, B.P., Garcia, S.P., Zaborowski, M.P., Solanes, P., Spataro, S., et al. (2019). Allele-specific gene editing prevents deafness in a model of dominant progressive hearing loss. Nat. Med. *25*, 1123–1130. https://doi.org/10.1038/s41591-019-0500-9.

Kazmierczak, P., Sakaguchi, H., Tokita, J., Wilson-Kubalek, E.M., Milligan, R.A., Müller, U., and Kachar, B. (2007). Cadherin 23 and protocadherin 15 interact to form tip-link filaments in sensory hair cells. Nature *449*, 87–91. https://doi.org/10.1038/nature06091.

Koblan, L.W., Erdos, M.R., Wilson, C., Cabral, W.A., Levy, J.M., Xiong, Z.M., Tavarez, U.L., Davison, L.M., Gete, Y.G., Mao, X., et al. (2021). In vivo base editing rescues Hutchinson-Gilford progeria syndrome in mice. Nature *589*, 608–614. https://doi.org/10.1038/s41586-020-03086-7.

Koike-Yusa, H., Li, Y., Tan, E.P., Velasco-Herrera, M.D.C., and Yusa, K. (2014). Genome-wide recessive genetic screening in mammalian cells with a lentiviral CRISPR-guide RNA library. Nat. Biotechnol. *32*, 267–273. https://doi.org/10.1038/nbt.2800.

Komor, A.C., Kim, Y.B., Packer, M.S., Zuris, J.A., and Liu, D.R. (2016). Programmable editing of a target base in genomic DNA without double-stranded DNA cleavage. Nature *533*, 420–424. https://doi.org/10.1038/nature17946.

Lee, Y.S., Liu, F., and Segil, N. (2006). A morphogenetic wave of p27Kip1 transcription directs cell cycle exit during organ of Corti development. Development *133*, 2817–2826. https://doi.org/10.1242/dev.02453.

Leenay, R.T., Aghazadeh, A., Hiatt, J., Tse, D., Roth, T.L., Apathy, R., Shifrut, E., Hultquist, J.F., Krogan, N., Wu, Z., et al. (2019). Large dataset enables prediction of repair after CRISPR-Cas9 editing in primary T cells. Nat. Biotechnol. *37*, 1034–1037. https://doi.org/10.1038/s41587-019-0203-2.

Li, J., Liu, S., Song, C., Hu, Q., Zhao, Z., Deng, T., Wang, Y., Zhu, T., Zou, L., Wang, S., et al. (2021). PIEZO2 mediates ultrasonic hearing via cochlear outer hair cells in mice. Proc. Natl. Acad. Sci. USA *118*, e2101207118. https://doi.org/10.1073/pnas.2101207118.

Meyers, J.R., MacDonald, R.B., Duggan, A., Lenzi, D., Standaert, D.G., Corwin, J.T., and Corey, D.P. (2003). Lighting up the senses: FM1-43 loading of sensory cells through nonselective ion channels. J. Neurosci. *23*, 4054–4065. https://doi.org/10.1523/jneurosci.23-10-04054.2003.

Murcia, C.L., and Woychik, R.P. (2001). Expression of Pcdh15 in the inner ear, nervous system and various epithelia of the developing embryo. Mech. Dev. *105*, 163–166. https://doi.org/10.1016/S0925-4773(01)00388-4.

Nishida, K., Arazoe, T., Yachie, N., Banno, S., Kakimoto, M., Tabata, M., Mochizuki, M., Miyabe, A., Araki, M., Hara, K.Y., et al. (2016). Targeted nucleotide editing using hybrid prokaryotic and vertebrate adaptive immune systems. Science *353*, aaf8729. https://doi.org/10.1126/science.aaf8729.

Nist-Lund, C.A., Pan, B., Patterson, A., Asai, Y., Chen, T., Zhou, W., Zhu, H., Romero, S., Resnik, J., Polley, D.B., et al. (2019). Improved TMC1 gene therapy restores hearing and balance in mice with genetic inner ear disorders. Nat. Commun. *10*, 236. https://doi.org/10.1038/s41467-018-08264-w.

Pan, B., Askew, C., Galvin, A., Heman-Ackah, S., Asai, Y., Indzhykulian, A.A., Jodelka, F.M., Hastings, M.L., Lentz, J.J., Vandenberghe, L.H., et al. (2017). Gene therapy restores auditory and vestibular function in a mouse model of Usher syndrome type 1c. Nat. Biotechnol. *35*, 264–272. https://doi.org/10.1038/nbt.3801.

Pawlowski, K.S., Kikkawa, Y.S., Wright, C.G., and Alagramam, K.N. (2006). Progression of inner ear pathology in Ames waltzer mice and the role of protocadherin 15 in hair cell development. J. Assoc. Res. Otolaryngol. *7*, 83–94. https://doi.org/10.1007/s10162-005-0024-5.

Platt, R.J., Chen, S., Zhou, Y., Yim, M.J., Swiech, L., Kempton, H.R., Dahlman, J.E., Parnas, O., Eisenhaure, T.M., Jovanovic, M., et al. (2014). CRISPR-Cas9 knockin mice for genome editing and cancer modeling. Cell *159*, 440–455. https://doi.org/10.1016/j.cell.2014.09.014.

Ran, F.A., Hsu, P.D., Wright, J., Agarwala, V., Scott, D.A., and Zhang, F. (2013). Genome engineering using the CRISPR-Cas9 system. Nat. Protoc. *8*, 2281–2308. https://doi.org/10.1038/nprot.2013.143.

Roman-Rodriguez, F.J., Ugalde, L., Alvarez, L., Díez, B., Diez, B., Ramírez, M.J., Ramirez, M.J., Risueño, C., Risueno, C., Cortón, M., et al. (2019). NHEJ-mediated repair of CRISPR-Cas9-induced DNA breaks efficiently corrects mutations in HSPCs from patients with Fanconi anemia. Cell Stem Cell *25*, 607–621.e7. https://doi.org/10.1016/j.stem.2019.08.016.

Schneider, C.A., Rasband, W.S., and Eliceiri, K.W. (2012). NIH Image to ImageJ: 25 years of image analysis. Nat. Methods *9*, 671–675. https://doi.org/10.1038/nmeth.2089.

Shen, M.W., Arbab, M., Hsu, J.Y., Worstell, D., Culbertson, S.J., Krabbe, O., Cassa, C.A., Liu, D.R., Gifford, D.K., and Sherwood, R.I. (2018). Predictable and precise template-free CRISPR editing of pathogenic variants. Nature *563*, 646–651. https://doi.org/10.1038/s41586-018-0686-x.

Stahl, J.S., van Alphen, A.M., and De Zeeuw, C.I. (2000). A comparison of video and magnetic search coil recordings of mouse eye movements. J. Neurosci. Methods *99*, 101–110. https://doi.org/10.1016/s0165-0270(00)00218-1.

Stemmer, M., Thumberger, T., Del Sol Keyer, M., Wittbrodt, J., and Mateo, J.L. (2015). CCTop: an intuitive, flexible and reliable CRISPR/Cas9 target prediction tool. PLoS One *10*, e0124633. https://doi.org/10.1371/journal.pone.0124633.

Stenson, P.D., Ball, E.V., Mort, M., Phillips, A.D., Shiel, J.A., Thomas, N.S., Abeysinghe, S., Krawczak, M., and Cooper, D.N. (2003). Human gene mutation database (HGMD): 2003 update. Hum. Mutat. *21*, 577–581. https://doi.org/10.1002/humu.10212.

Suzuki, K., Tsunekawa, Y., Hernandez-Benitez, R., Wu, J., Zhu, J., Kim, E.J., Hatanaka, F., Yamamoto, M., Araoka, T., Li, Z., et al. (2016). In vivo genome editing via CRISPR/Cas9 mediated homology-independent targeted integration. Nature *540*, 144–149. https://doi.org/10.1038/nature20565.

Suzuki, K., Yamamoto, M., Hernandez-Benitez, R., Li, Z., Wei, C., Soligalla, R.D., Aizawa, E., Hatanaka, F., Kurita, M., Reddy, P., et al. (2019). Precise in vivo genome editing via single homology arm donor mediated intron-targeting gene integration for genetic disease correction. Cell Res. *29*, 804–819. https://doi.org/10.1038/s41422-019-0213-0.

Symington, L.S., and Gautier, J. (2011). Double-strand break end resection and repair pathway choice. Annu. Rev. Genet. *45*, 247–271. https://doi.org/10.1146/annurev-genet-110410-132435.

van Overbeek, M., Capurso, D., Carter, M.M., Thompson, M.S., Frias, E., Russ, C., Reece-Hoyes, J.S., Nye, C., Gradia, S., Vidal, B., et al. (2016). DNA repair profiling reveals nonrandom outcomes at Cas9-mediated breaks. Mol. Cell *63*, 633–646. https://doi.org/10.1016/j.molcel.2016.06.037.

Walton, R.T., Christie, K.A., Whittaker, M.N., and Kleinstiver, B.P. (2020). Unconstrained genome targeting with near-PAMless engineered CRISPR-Cas9 variants. Science *368*, 290–296. https://doi.org/10.1126/science.aba8853.

Webb, S.W., Grillet, N., Andrade, L.R., Xiong, W., Swarthout, L., Della Santina, C.C., Kachar, B., and Müller, U. (2011). Regulation of PCDH15 function in mechanosensory hair cells by alternative splicing of the cytoplasmic domain. Development *138*, 1607–1617. https://doi.org/10.1242/dev.060061.

Xiong, W., Wagner, T., Yan, L., Grillet, N., and Müller, U. (2014). Using injectoporation to deliver genes to mechanosensory hair cells. Nat. Protoc. *9*, 2438–2449. https://doi.org/10.1038/nprot.2014.168.

Yang, X., Zhou, S., Wu, J., Liao, Q., Wang, C., Liu, M., Qu, L., Zhang, Y., Cheng, C., Chai, R., et al. (2019). Surgery-free video-oculography in mouse models: enabling quantitative and short-interval longitudinal assessment of vestibular function. Neurosci. Lett. *696*, 212–218. https://doi.org/10.1016/j.neulet.2018.12.036.

Yang, Y., Liu, N., He, Y., Liu, Y., Ge, L., Zou, L., Song, S., Xiong, W., and Liu, X. (2018). Improved calcium sensor GCaMP-X overcomes the calcium channel perturbations induced by the calmodulin in GCaMP. Nat. Commun. *9*, 1504. https://doi.org/10.1038/s41467-018-03719-6.

Yao, X., Wang, X., Hu, X., Liu, Z., Liu, J., Zhou, H., Shen, X., Wei, Y., Huang, Z., Ying, W., et al. (2017). Homology-mediated end joining-based targeted integration using CRISPR/Cas9. Cell Res. *27*, 801–814. https://doi.org/10.1038/cr.2017.76.

Yeh, W.H., Shubina-Oleinik, O., Levy, J.M., Pan, B., Newby, G.A., Wornow, M., Burt, R., Chen, J.C., Holt, J.R., and Liu, D.R. (2020). In vivo base editing restores sensory transduction and transiently improves auditory function in a mouse model of recessive deafness. Sci. Transl. Med. *12*, eaay9101. https://doi.org/10.1126/scitranslmed.aay9101.

Yu, Q., Wang, Y., Chang, Q., Wang, J., Gong, S., Li, H., and Lin, X. (2014). Virally expressed connexin26 restores gap junction function in the cochlea of conditional Gjb2 knockout mice. Gene Ther. *21*, 71–80. https://doi.org/10.1038/gt.2013.59.

Zhao, B., Wu, Z., Grillet, N., Yan, L., Xiong, W., Harkins-Perry, S., and Müller, U. (2014). TMIE is an essential component of the mechanotransduction machinery of cochlear hair cells. Neuron *84*, 954–967. https://doi.org/10.1016/j.neuron.2014.10.041.

STAR★METHODS

KEY RESOURCES TABLE

REAGENT or RESOURCE	SOURCE	IDENTIFIER
Antibodies		
Rabbit anti-PCDH15 (PB811)	Dr. Ulrich Müller	N/A
Rabbit polyclonal anti-Myo7a	Proteus Biosciences	Cat#25-6790; RRID:AB_10015251
goat anti-rabbit Alexa 647 conjugated	Thermo Fisher	Cat#A-21245; RRID:AB_2535813
Bacterial and virus strains		
AAV-mCherry	Vigene Bioscience	N/A
AAV-m-*3j*-gRNA1	Vigene Bioscience	N/A
Chemicals, peptides, and recombinant proteins		
Ampicillin	TransGen Biotech	Cat#GG101
tribromoethanol	Sigma-Aldrich	Cat#T48402
Fast green	Sigma-Aldrich	Cat#F7258
EGTA	Sigma-Aldrich	Cat#E3889; CAS: 67-42-5
bovine serum albumin	Sigma-Aldrich	Cat#A3059; CAS: 9048-46-8
Phalloidin Alexa Fluor 488	Thermo Fisher	Cat#A12379
Phalloidin Alexa Fluor 568	Thermo Fisher	Cat#A12380
FM5-95	Thermo Fisher	Cat#T23360
T4 Polynucleotide Kinase	NEB	Cat#M0201S
BbsI	NEB	Cat#R0539S
collagenase I	Sigma-Aldrich	Cat#C0130-1g
QuickExtract™ DNA Extraction Solution 1.0	Lucigen	Cat#QE09050
Kapa HiFi 2 x master mix	Kapa Biosystems	Cat#KK2601
T4 ligase	Invitrogen	Cat#15224017
Phosphate buffered saline	Leagene	Cat#cc0005
4% paraformaldehyde	Leagene	Cat#DF0135
ProLong Gold Antifade Mountant	Thermo Fisher	Cat#P36930
Qubit™ 1× dsDNA HS Assay Kit	Thermo Fisher	Cat#Q33230,
0.05% trypsin-EDTA	Thermo Fisher	Cat#25200056
DMEM/F12 medium	Thermo Fisher	Cat#21041-025
HBSS	Thermo Fisher	Cat#C14175500CP
Critical commercial assays		
Gel Purification kit	Magen	Cat#D2110
MaxPure Plasmid HC kit	Magen	Cat#P1231
Experimental models: Organisms/strains		
Mouse: C57BL/6J-*Pcdh15*$^{av-3J}$/J	Alagramam et al., 2001	JAX: 002072
Mouse: Gt(ROSA)26Sor$^{tm1.1(CAG-Cas9*-EGFP)Fezh}$	Platt et al., 2014	JAX: 024858
Mouse: C57B6J	The Jackson Laboratory	JAX:000664
Oligonucleotides		
See Table S3 for oligonucleotide information	N/A	N/A
Recombinant DNA		
Plasmid: PX330	Addgene	Cat#42230
Plasmid: pcDNA3.1(-)-PCDH15-CD2	This paper	N/A
Plasmid: pN1-GCaMP6m-XC	Addgene	Cat#111543
Plasmid: pcDNA3.1(-)-PCDH15-E1373R	This paper	N/A

(*Continued on next page*)

Continued

REAGENT or RESOURCE	SOURCE	IDENTIFIER
Plasmid: pcDNA3.1(-)-PCDH15-E1373del	This paper	N/A
Plasmid: pcDNA3.1(-)-PCDH15-E1373RK	This paper	N/A
Software and algorithms		
CCtop (CRISPR-Cas9 target online predictor)	Stemmer et al., 2015	https://crispr.cos.uni-heidelberg.de
CRISPResso2 v.2.0.32	Clement et al., 2019	https://github.com/pinellolab/CRISPResso2
Huygens deconvolution 18.10	SVI	https://svi.nl/Huygens-Deconvolution
Imaris Software 9.3.1	Oxford Instrument	https://imaris.oxinst.com/
Micro-Manager 1.6	Micro-Manager	https://micro-manager.org/
ImageJ	Schneider et al., 2012	https://imagej.nih.gov/ij/
Excel 2019	Microsoft	https://www.microsoft.com/zh-cn/microsoft-365/excel
Cas-OFFinder	Bae et al., 2014	http://www.rgenome.net/cas-offinder/
Zeiss Black software	Zeiss	https://www.zeiss.com/microscopy/int/products/microscope-software/
The EthoVision XT version 11.5	Noldus Information Technology	https://www.noldus.com/ethovision-xt
GraphPad Prism 6	GraphPad Software	https://www.graphpad.com/scientific-software/prism/

RESOURCE AVAILABILITY

Lead contact

Further information and requests for resources and reagents should be directed to and will be fulfilled by the lead contact, Wei Xiong (wei_xiong@tsinghua.edu.cn).

Materials availability

Plasmids generated in this study would be deposited to Addgene.

Data and code availability

- The paper does not report single-cell RNA-seq data and western blot images. Microscopy data reported in this paper will be shared by the lead contact upon request.
- The paper does not report original code.
- Any additional information required to reanalyze the data reported in this paper is available from the lead contact upon request.

EXPERIMENTAL MODEL AND SUBJECT DETAILS

All animal experiments were performed in compliance with the guidelines provided by the Institutional Animal Care and Use Committee (IACUC) at Tsinghua University. The mice were maintained in the Animal Research Facility in campus, accredited by the Association for Assessment and Accreditation of Laboratory Animal Care International (AAALAC). The *av3j/av3j* mice (Alagramam et al., 2001) (C57BL/6J-*Pcdh15*$^{av-3J}$/J, JAX:002072) were provided by Dr. Ulrich Müller at Johns Hopkins University. The *av3j/av3j;Cas9+* mice were obtained by crossing *av3j/av3j* mice with the Cas9 knockin mice (Platt et al., 2014) (Gt(ROSA)26Sor$^{tm1.1(CAG-Cas9*-EGFP)Fezh}$, JAX:024858). The mice were housed in a temperature-controlled room with 12-hr light/dark cycle and had free access to water and food. Both female and male mice were used throughout the study.

METHOD DETAILS

Design of gRNAs and plasmid construction

All gRNAs were constructed using the PX330 backbone (42230, Addgene). The primers used for plasmid construction were designed by CCtop (CRISPR-Cas9 target online predictor, https://crispr.cos.uni-heidelberg.de) (Stemmer et al., 2015) with all default parameters, except the gRNA length was adjusted to 17 nt. The plasmids were constructed as reported in prior research (Ran et al., 2013). The oligos were phosphorylated by T4 Polynucleotide Kinase (M0201S, NEB) at 37°C for 30 min, then annealed by temperature ramping from 95°C to 25°C in a thermocycler. The PX330 backbone was digested with BbsI (R0539S, NEB) and ligated with the oligos

using T4 ligase (15224017, Invitrogen). Plasmids were extracted using a MaxPure Plasmid HC kit (P1231, Magen, China) for subsequent procedures including cell-line transfection and tissue electroporation. PCDH15-CD2 cDNA (NCBI Reference Sequence: NM_001142742.1) was cloned in the pcDNA3.1 vector and driven by CMV promoter, which was further engineered to PCDH15-E1373R, PCDH15-E1373del, and PCDH15-E1373RK, respectively.

Cochlear tissue culture and injectoporation

Cochlear culture and injectoporation were performed as described in our previous study (Xiong et al., 2014). In this study, the organ of Corti was dissected from P0–P2 mouse pups and was attached on the inner side of a 35-mm culture dish lid (tissue culture dish) containing 2 mL DMEM/F12 medium (21041-025, Thermo Fisher) with ampicillin (1.5 μg/mL, GG101, TransGen Biotech). The dish lid was used to support the culture because the lid rim provided better accessibility for electroporation electrodes. A 60-mm culture dish filled with 1 mL sterile H_2O (housing dish) housed up to 3 tissue culture dishes, which maintained the humidity. After 6-hr of culturing in a humid incubator (150i, Thermo Fisher) (37°C, 5% CO_2), the cochlear tissues were ready for electroporation. A pair of electroporation electrodes was created using 0.4-mm diameter platinum wire and shaped like a hockey stick, which were positioned in parallel and spaced by a 2-mm distance. We used an upright microscope (Olympus BX51WI) equipped with 5× and 60× objectives to assist with placing the cochlea fragments precisely between the electroporation electrodes. For electroporation, plasmids (1 μg/μL in HBSS, pH 7.4, with higher osmolality at 360 mOsm/L adjusted by 10× HBSS) were centrifuged at 12000 g for 10 min at 4°C before they were injected into gaps between hair cells via a glass electrode with an open tip of 2 μm diameter. To avoid contamination, the injection electrode was pre-washed with 75% alcohol and backfilled with the plasmid solution using a 2 μL pipette with a long tip. After puncturing into the reticular laminar, the glass injection electrode was applied using 0.1 mL of compressed air through a 1 mL syringe for 15 s to diffuse plasmids, driving OHCs waving as observed with the 60× objective (Movie S1). A series of 3 square electrical pulses (80-V amplitude, 20-ms duration, 1-s interval) was immediately applied using an electroporator (BTX ECM830, Harvard Apparatus). After lifting the objective off the medium, the electroporation was conducted directly in the tissue culture dish. After electroporation, 50% of the culture medium volume was replaced with fresh medium and the tissues were cultured for up to 4 days. The culture medium in tissue culture dishes and sterile water in housing dishes were supplied every day during tissue culture. At designated time points, transfected tissues were used for either immunofluorescence or Ca^{2+} imaging.

Tissue digestion and FACS

Injectoporated or AAV-transfected auditory tissues (containing basilar membrane, spiral ligament, and stria vascularis) and vestibular tissues (include utricles, saccules, and semicircular canals) were rapidly dissected in ice-cold HBSS (C14175500CP, Thermo Fisher) and incubated in HBSS with 1 mg/mL collagenase I (C0130-1g, Sigma-Aldrich) and 0.05% trypsin-EDTA (25200056, Thermo Fisher) at 34°C for 10–15 min. The effect of enzymatic dissociation was verified using an inverted microscope. An equal volume of 10% FBS-containing DMEM/F-12 medium was added to halt the reaction. After centrifuging at 1,000 g for 1min, the cells were washed with 10% FBS-containing DMEM/F-12 and re-suspended. After passing through a 70-μm filter to remove large debris, the isolated cells were sorted with fluorescence signals and enriched directly into 0.2-μL PCR tubes by a FACS machine (BD Influx). In order to get enough cells for downstream sequencing, the FACS gate was relatively loose to collect total cells containing red cells at 5–20%.

DNA sequencing library construction

Genome DNA of transfected tissue cells were extracted using the QuickExtract™ DNA Extraction Solution 1.0 (QE09050, Lucigen, Middleton, WI) and following the manufacturer's directions. For each targeting genome locus, an amplicon of 100–300 bp was designed, with cleavage sites located approximately 50–100bp away from the amplicon boundaries. The first run of PCR (PCR1) was applied to amplify targeting DNA with primers containing part of the Illumina adaptors. Exonuclease I was added to the PCR1 products to clear all remaining PCR1 primers. A second run of PCR was performed to add unique barcodes and P5/P7 flow cell binding sites. All PCR reactions were carried out using Kapa HiFi 2 x mastermix (KK2601, Kapa Biosystems). PCR products were then separated using a 2% agarose gel, and a subset of select sizes were cut and purified using a Gel Purification kit (D2110, Magen, China). After being quantified using Qubit™ 1× dsDNA HS Assay Kit (Q33230, Thermo Fisher) and verified by Agilent 2100 Bioanalyzer, samples were pooled together and sequenced 2 × 150 on the Illumina HiSeq X-Ten platform.

Immunofluorescence

For PCDH15 immunostaining, cultured or fresh dissected cochlear tissues were pre-treated with phosphate buffered saline (PBS, cc0005, Leagene; calcium free), adding 5 mM EGTA (E3889, Sigma-Aldrich) for 10 min at room temperature (RT), then fixing the tissues in 4% paraformaldehyde (PFA, DF0135, Leagene) for 10 min at RT. We washed the tissues for 5 min × 3 times and blocked in 1% bovine serum albumin (BSA, A3059, Sigma-Aldrich) (w/v) for 1 hour at RT before incubating with antibodies. The primary antibody was rabbit anti-PCDH15 (PB811, 1:400 dilution, a gift kindly provided by Dr. Ulrich Müller), incubated at 4°C for 16 hours followed by 15 min × 3 times washed in PBS. The secondary antibodies were goat anti-rabbit (A-21245, Alexa 647 conjugated, Thermo Fisher, 1:500) with either Alexa Fluor 488 (A12379, Thermo Fisher, 1:1000) or Alexa Fluor 568 Phalloidin (A12380, Thermo Fisher, 1:1000), incubated at RT for 2 hours followed by 15 min × 3 times washed in PBS. All antibodies were diluted in PBS using 5 mM EGTA

by v/v. The tissues were finally mounted with ProLong Gold Antifade Mountant (P36930, Thermo Fisher). Images were acquired using a deconvolution microscope (DeltaVision, Applied Precision) equipped with a 100x oil-immersed objective and deconvolved using the Huygens deconvolution software (version 18.10, SVI).

For virus transfection and hair cell survival quantification, animals were sacrificed and the inner ear tissues were harvested. The tissues were fixed in 4% PFA for 30min at RT and washed in PBS for 7 min × 3 times. We dissected the basilar membrane and blocked in 1% BSA for 1 hour at RT before incubating with antibodies. The primary antibody was rabbit anti-Myo7a (25–6790, Proteus Biosciences Inc, 1:1000) incubated at 4°C overnight and followed by 15 min × 3 times washed in PBS. The secondary antibodies were goat anti-rabbit Alexa 647 conjugated at 1:2000 with Alexa Fluor 488 Phalloidin (1:1000). Finally, the tissues were mounted with ProLong Gold Antifade Mountant. Images were captured using Andor Dragonfly spinning disk confocal microscopy using the 40× oil-immersed objective. The spot and filament function of Imaris Software v9.3.1 (Oxford Instrument) were used for cell number quantification. For virus transfection quantification, gamma values were set to 3 in order to show clear labeling of weak viral expression cells.

Cochlea calcium imaging

The genetically encoded Ca^{2+} indicator GCaMP6m-X (Yang et al., 2018) was co-transfected with other plasmids in cochlear hair cells using tissue culture and injectoporation techniques described above. For calcium imaging, the tissues were bathed in fresh external solution (in mM): 144 NaCl, 5.8 KCl, 2.5 $CaCl_2$, 0.9 $MgCl_2$, 10 HEPES, 5.6 D-Glucose, PH7.4. We used an upright microscope (BX51WI, Olympus) mounted with an LED light source (Lambda HPX LED, Sutter Instrument) and an sCMOS camera (ORCA Flash 4.0, Hamamatsu) controlled by Micro-Manager 1.6 software (Edelstein et al., 2010). A series of three fluid-jet stimuli (20 psi, 0.1 s, 0.3 s and 0.5 s) were applied through a glass capillary with an open tip of 5 μm diameter at 40-s interval. Images were acquired at a 2-s sampling rate with a 60× water-immersed objective.

Virus injection

All AAVs used in this study were customized from Vigene Bioscience, Jinan, China. For anesthesia, P0–P2 mice were put on ice and waited for 1–2 min. A dorsal incision was made and the bulla in the ear was exposed. Using a stereotaxic microscope, the scala media was visually located between the round widow niche and the stapedial artery, and 600-nL of virus solution (1.5×10^{14} vg/mL) was injected into the scala media at a rate of 250 nL/min. Fast green (F7258, Sigma-Aldrich) was added to monitor the delivery effect until successful delivery to the scala media was signaled by the formation of a ribbon pattern. For each pup, both ears were injected and all procedures were completed within 20 min. The injected pups were placed on an electric blanket until they were revived, and returned to the mother mice.

Off-target prediction

Mismatch off-targets were predicted using CCtop (CRISPR-Cas9 target online predictor, https://crispr.cos.uni-heidelberg.de). All mismatched off targets were ranked by number of mismatches, then the off-target loci were chosen using different alignment parameters. Off targets with DNA bulges were identified using Cas-OFFinder (Bae et al., 2014) (http://www.rgenome.net/cas-offinder/), and we set the DNA bulge size to 1bp. Off-target loci with different bulge locations were selected (Tables S2 and S3). All selected bulge loci also exhibited a 1 bp mismatch compared to the on-target site. All off-targets avoided the repeating region.

Whole-cell electrophysiology of hair cells

At assigned ages, the mice were sacrificed and the apex of the basilar membrane or entire saccules were removed and transferred to the dissection solution, containing (in mM): 5 KCl, 140 NaCl, 1 $MgCl_2$, 0.5 $MgSO_4$, 0.1 $CaCl_2$, 10 HEPES, 3.4 L-Glutamine, and 10 D-Glucose; pH 7.2. The tectorial membrane or otolith was removed using fine forceps, and the organ of Corti or sacculus was transferred to a dish with recording solution, containing (in mM): 145 NaCl, 0.7 NaH_2PO_4, 5 KCl, 1.3 $CaCl_2$, 0.9 $MgCl_2$, 10 HEPES, and 5.6 D-Glucose; pH 7.4. mCherry expressed OHCs or VHCs were whole-cell recorded and membrane currents were measured using an electrophysiology amplifier (EPC-10 USB, HEKA, Germany) at a sampling rate of 20 kHz. The cells were held at −70 mV and the hair bundle was stimulated using a fluid jet. A 40-Hz sinusoid was applied to OHCs and IHCs for 60 ms. Compared to stimuli applied to OHCs, the fluid-jet driving voltage was set lower in order to avoid IHC hair bundle damage. For VHCs, a 500-ms square wave was applied to sufficiently stimulate the hair cells.

FM5-95 loading and imaging

Wild-type C57B6J animals and *av3j/av3j;Cas9+* animals with and without virus injections were sacrificed at P7–P10. Basilar membranes were dissected in 1× HBSS and bathed in 6μM ice-cold FM5-95 (T23360, Thermo Fisher, dissolved in 1× HBSS) for 30s, followed by 4–5 washes in clean HBSS. Tissues were attached to the underside of a glass bottom dish using prolong-antifade solution. Images were obtained using a Zeiss LSM880 confocal microscope equipped with standard laser lines (405, 514, 561, 633 nm) using 40× (NA 1.2) water-immersion objective. Maximum projections of z-stacks were handled using Zeiss Black software. FM5-95 was stimulated using a 514-nm laser and monitored in the 680–742nm region, an emission wavelength to distinguish the GFP signal (Cas9 knockin) and mCherry signal from the virus.

Auditory brainstem response (ABR)

Mice were anesthetized by administering an intraperitoneal injection of tribromoethanol (300 mg/kg). ABR experiments were performed in a commercial soundproof chamber manufactured by Shanghai Shino Acoustic Equipment Co., Ltd (Li et al., 2021). Animals were placed on an electric blanket to maintain body temperature. The recording electrode was inserted beneath the scalp between the two ears. The reference electrode and the ground electrode were inserted subcutaneously at the pinna and the groin respectively. The ABR data were collected through an RZ6 workstation controlled using BioSig software (Tucker-Davis Technologies, Alachua, FL), where sound stimulation calibration was completed on each experimental day using the PCB piezotronics microphone set provided in the TDT RZ6 system. Clicks and 4–32 kHz pure-tone bursts were generated by a TDT MF1 open-field magnetic speaker. Balanced click stimuli with a duration of 0.1 ms were given at a rate of 21 Hz. As for pure tone stimuli, 5.6 kHz, 8 kHz, 11.3 k Hz, 16 kHz, 22.6 kHz, or 32 kHz sine tone pips with a 5-ms duration (gate type of Cos2, frequency 21 Hz) were applied to the ears. Maximum stimulus intensity was set to a 110 dB sound pressure level (SPL). The sound levels decreased in 5 dB steps from 110 dB SPL and in 10 dB steps below threshold. For each stimulus, electroencephalographic activity was recorded for 10 ms at sampling rate of 25 kHz (filtered 100 Hz to 3 kHz). Following each acoustic stimulation, 512 or 1024 responses were captured and averaged. The ABR threshold was defined visually as the lowest SPL level at which any wave could be detected and reproduced with increasing sound intensities. To enable average and statistical measures, in animals with no response at 110 dB SPL, the ABR threshold was established at 115 dB SPL.

Acoustic startle response

Acoustic startle responses were recorded by Xeye Startle Reflex system (v1.2, Beijing MacroAmbition S&T Development). The animals were tested in a sound shielded startle box and startle responses were sensed by the gravitational acceleration sensor fixed beneath an elevated platform. Mice were placed in a smaller, square, plastic chambers and anchored to the sensing platform during recording. The experiment began with a 5 min 60 dB SPL background white noise followed by 32 trials of single noise pulses presented in a pseudorandom order at randomized inter-trial intervals between 10-50s (90 to 120 dB SPL with 10 dB steps, 40 ms duration with 0 ms onset and offset ramps). A fan was switched on and placed outside the startle box throughout the experiment to reduce external noise interference. We recorded eight repetitions at each sound intensity for each subject.

Vestibulo-ocular reflex (VOR)

The VOR recording were conducted as reported in a previous study (Yang et al., 2019). Within a metal chamber, the mouse was immobilized using a clamp and mounted on a mirror-camera-equipped turn table. Binocular eye movements were evoked through $\pm 20^{\circ}$ sinusoidal rotations at 0.25, 0.5, or 1 Hz frequencies. For each animal, a 2–3 min video was recorded and traced using custom machine-learning-based scripts in MATLAB R2016a.

Open field test

4- to 8-week-old animals were included in all behavioral tests carried out in a 33 × 33 cm arena with infrared illumination, which was cleaned between animals. The animals were placed on one side of the arena and recorded for 10 min. Circling behaviors were quantified using a behavior analysis software (The EthoVision XT version 11.5, Noldus Information Technology). Both clockwise and anticlockwise circling were counted in the analysis of circling frequency and moving traces were tracked using custom MATLAB scripts.

Rotarod test

Animals were first trained on a rotarod (47650, Ugo Basile) 5 times over 2 days, in which the first two training sessions included a constant 10 rpm for 1–2 min. The following three training sessions included 300-s test trials that began at 10 rpm and increased to 30 rpm over 90 s, then continued rotating at 30 rpm over 300 s. During test phase, each animal ran 5 times before it fell from the rotarod. After excluding maximum and minimum times, the average running time was subsequently used for data analysis.

QUANTIFICATION AND STATISTICAL ANALYSIS

Bioinformatic analysis

Sequencing reads were demultiplexed according to the 8-nt index sequence and then individual FASTQ files were analyzed using the batch version of CRISPResso2 v.2.0.32 (Clement et al., 2019) with the CRISPRessoPooled mode. The analysis parameters were set to: -w 12, -q 30, -s 0, –max_paired_end_reads_overlap 150, and the remaining parameters were set to the default setting. All other analysis and quantification were based on the "Alleles_frequency_table.txt" in the CRISPResso2 report using custom Python scripts or Excel2016. Our editing analyses exclude reads with only substitutions. The indel frequencies were calculated as follows:

$$\frac{\text{all edited reads} - \text{substitution only reads}}{\text{all reads for the target locus}}$$

Ca^{2+} imaging data analysis

The Ca^{2+} imaging data were analyzed offline using ImageJ (NIH) and Excel (Microsoft) software. The fluorescence intensity (F) of the hair-cell soma was measured to generate a time-lapsed trace. Relative fluorescence changes ($\Delta F/F_0$) were calculated by normalizing F to the fluorescence intensity of the first frame (F_0) using the equation:

$$\frac{\Delta F}{F0} = \frac{F - F0}{F0}.$$

Fluorescence changes from cells within the same condition were averaged.

VOR analysis

The degree of horizontal eye-move was calculated using the equation:

$$\alpha = \frac{EH \cdot 180}{pi \cdot RP}$$

α indicates horizontal eye-movement degree, EH indicates horizontal eye-movement distance, pi is the Constant of PI, and RP indicates the axial length of eye movements (Stahl et al., 2000). Six periods, whose peak frequency coincided with the stimulus frequency, were averaged to calculate the final eye movement angles. The gain value was calculated as:

$$\text{Gain} = \frac{\text{Eye movement angle}}{\text{Platform stimulation angle}}.$$

Statistical analysis

Number of samples, replicates, and experiments are listed in Table S4. To compare between WT control, treated, and untreated groups, we used a Brown-Forsythe and Welch ANOVA test. $p < 0.05$ was considered significant and the labeling of statistical significance was designated as *$p < 0.05$, **$p < 0.01$, ***$p < 0.001$, ****$p < 0.0001$. GraphPad Prism 6 (GraphPad Software, San Diego, CA) were used for all statistical analyses.

Cell Reports, Volume *40*

Supplemental information

Template-independent genome editing in the *Pcdh15*$^{av-3j}$ mouse, a model of human DFNB23 nonsyndromic deafness

Lian Liu, Linzhi Zou, Kuan Li, Hanqing Hou, Qun Hu, Shuang Liu, Jie Li, Chenmeng Song, Jiaofeng Chen, Shufeng Wang, Yangzhen Wang, Changri Li, Haibo Du, Jun-Liszt Li, Fangyi Chen, Zhigang Xu, Wenzhi Sun, Qianwen Sun, and Wei Xiong

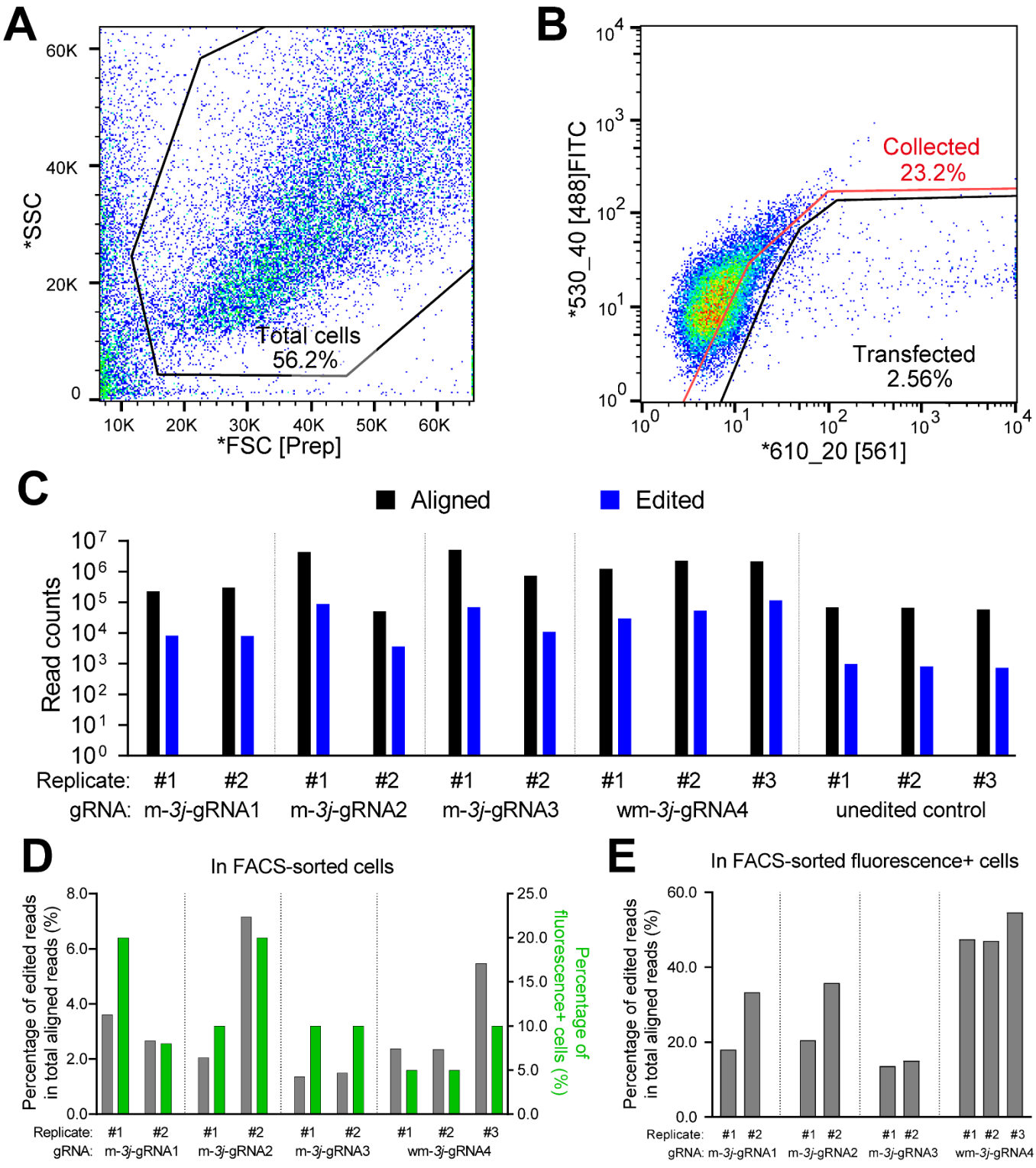

Figure S1. Cell sorting and editing fractions of the gRNA-injectoporated cochlear tissues, related to Figure 1. (A-B) An example showing FACS collection of the injectoporated cochlear cells. In the digested cochlear preparations, the total live cells occupy 56.2% of the contents (A), and 23.2% of the cells were collected for amplicon sequencing (B, within red gate), and transfected cells were only in a

fraction of 2.56% (B, within black gate) that is 11% of the collected cells. For FACS sorting of the injectoporated cells, the transfected cells usually occupied 5-20% of the total collected cells. Normally, we could get around 500 injectoporated cells from each injectoporated cochlea. (C) Number of aligned and edited reads. All ex vivo samples used in this study are shown per replicate and per gRNA. (D-E) Fractions of the edited reads in the total aligned reads before (D) and after (E) corrected by the transfection rates (green bars in D), shown per replicate and per gRNA. Take the m-*3j*-gRNA1 replicate #1 for example, the transfected cells occupy 20% of the total sorted cells that generated 3.6% of the edited reads in the total aligned reads. Thus in theory, the percentage of the actual edited reads is 3.6%/20% that equals to 18%.

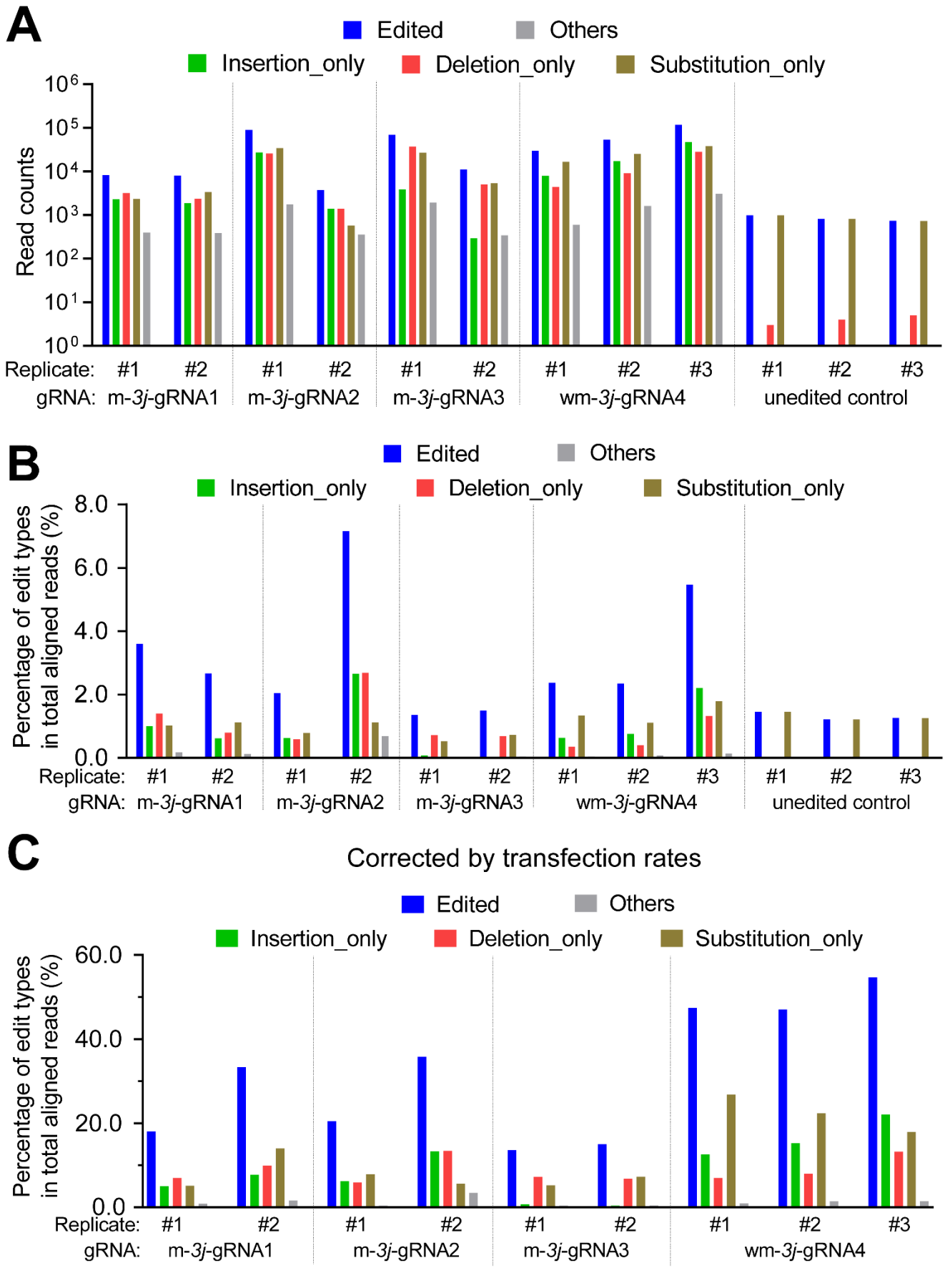
A
Edited
Others
Insertion_only
Deletion_only
Substitution_only
Read counts
10^6
10^5
10^4
10^3
10^2
10^1
10^0
Replicate: #1 #2 #1 #2 #1 #2 #1 #2 #3 #1 #2 #3
gRNA: m-3j-gRNA1 m-3j-gRNA2 m-3j-gRNA3 wm-3j-gRNA4 unedited control
B
Edited
Others
Insertion_only
Deletion_only
Substitution_only
Percentage of edit types in total aligned reads (%)
8.0
6.0
4.0
2.0
0.0
Replicate: #1 #2 #1 #2 #1 #2 #1 #2 #3 #1 #2 #3
gRNA: m-3j-gRNA1 m-3j-gRNA2 m-3j-gRNA3 wm-3j-gRNA4 unedited control
C
Corrected by transfection rates
Edited
Others
Insertion_only
Deletion_only
Substitution_only
Percentage of edit types in total aligned reads (%)
60.0
40.0
20.0
0.0
Replicate: #1 #2 #1 #2 #1 #2 #1 #2 #3
gRNA: m-3j-gRNA1 m-3j-gRNA2 m-3j-gRNA3 wm-3j-gRNA4

Figure S2. Analysis of edit types in the gRNA-injectoporated cochlear cells, related to Figure 1. (A) Number of reads classified by editing types. All ex vivo samples used in this study are shown per replicate and per gRNA. (B-C) The percentages of different types of editing in the total aligned reads before (B) and after (C) corrected by the transfection rates (Figure S1D, green bars).

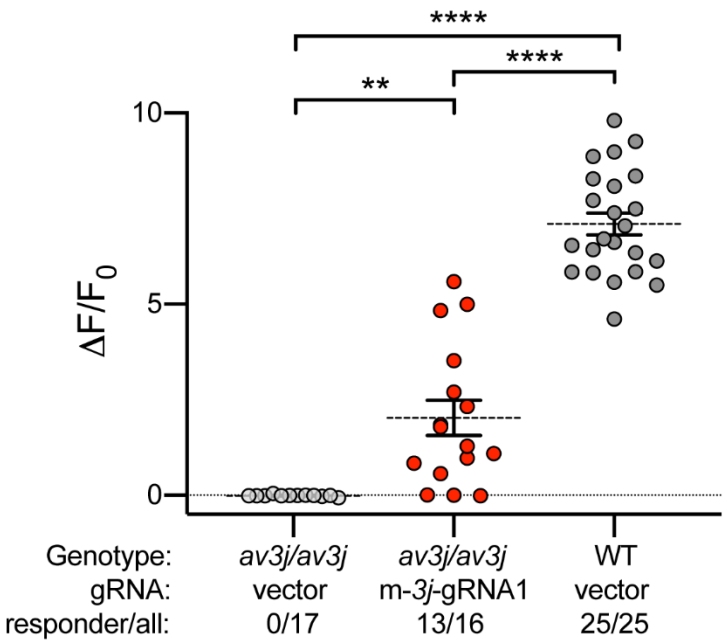

Figure S3. Ex vivo m-*3j*-gRNA1 injectoporation partially restores mechanotransduction in the *av3j/av3j* IHCs, related to Figure 2. Quantification of the maximal Ca^{2+} responses activated by fluid-jet stimuli in *av3j/av3j* IHCs or WT IHCs injectoporated by control PX330 vector or PX330-m-*3j*-gRNA1 (P1+4 DIV). Responsive and total recorded cell numbers are shown in panels. Brown-Forsythe and Welch ANOVA test; ns, no significance, $^{**}P < 0.01$, $^{****}P < 0.0001$, error bars, SEM.

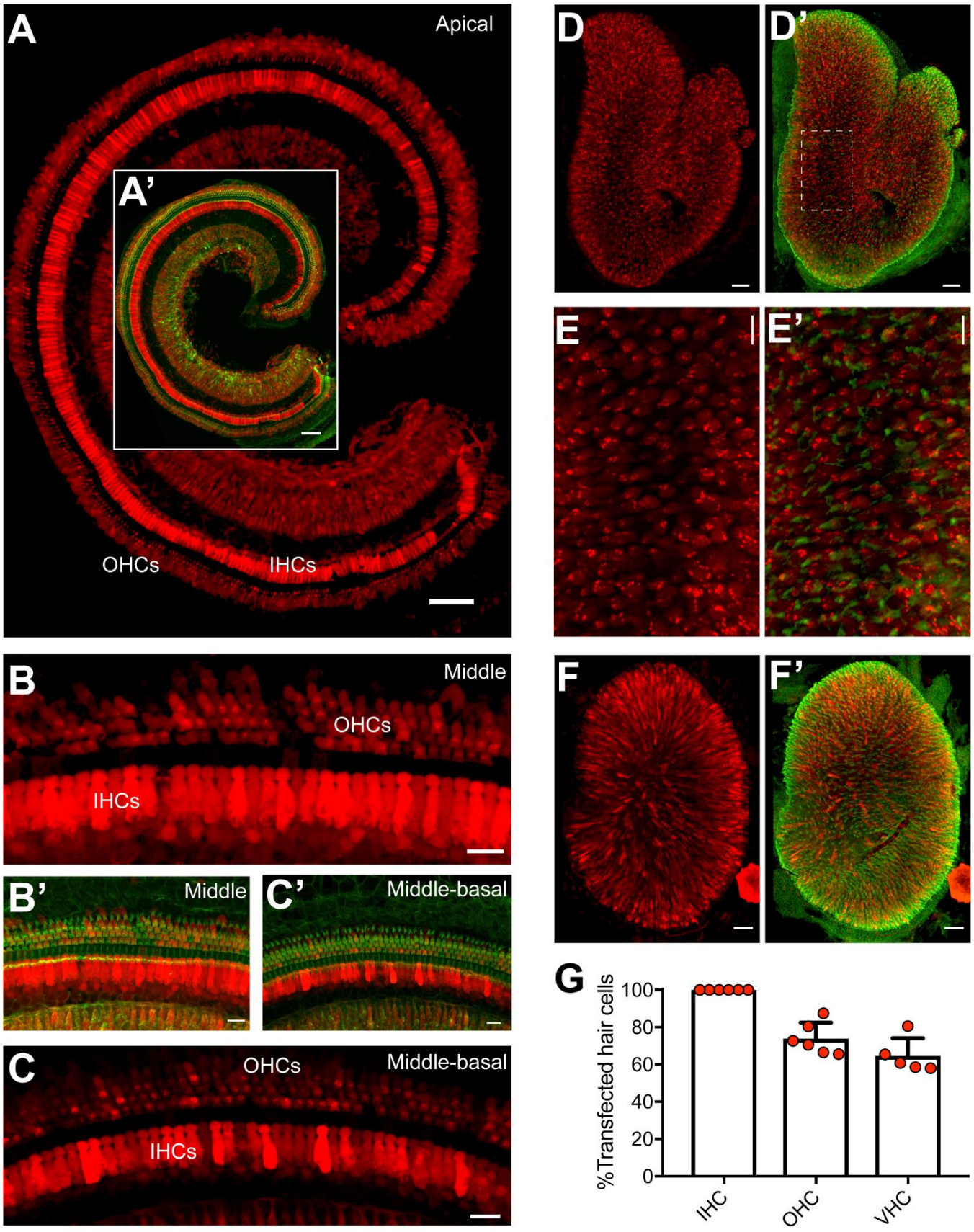
A
Apical
A'
OHCs
IHCs
B
Middle
OHCs
IHCs
B'
Middle
C'
Middle-basal
C
OHCs
Middle-basal
IHCs
D
D'
E
E'
F
F'
G
%Transfected hair cells
100
80
60
40
20
0
IHC
OHC
VHC

Figure S4. In vivo AAV-m-*3j*-gRNA1 transduction efficiency in the auditory and vestibular sensory epithelia, related to Figure 4. (A-C) Representative photos of the cochleae in WT mice at 14 days PVD. Hair bundles were stained with phalloidin (green), and virus transfection was illustrated by the mCherry (red). Apical (A), Middle (B), and middle-basal (C) coils are shown in high magnification. (A'), (B'), and (C') are lower-magnification two-channel merged views. (D and E) Low-magnification (D) and high-magnification (E, white dashed frame in D') views of the utricles from the same animal described in (A-C). (F) The virus transfection in saccule from mice with the same injection condition in (A). (D'), (E'), and (F') are two-channel merged views. (G) Quantification of virus transduction efficiencies of hair cells in the cochleae (n=6) and the vestibular organs (n=5). Each dot represents one transfected tissue. Scale bar, (A) 100 μm, (B and C) 20 μm, (D-F) 50 μm. In order to show the accurate transfection efficiency in all hair cells, gamma values were set to 3, for the large variations of virus-mediated protein expression.

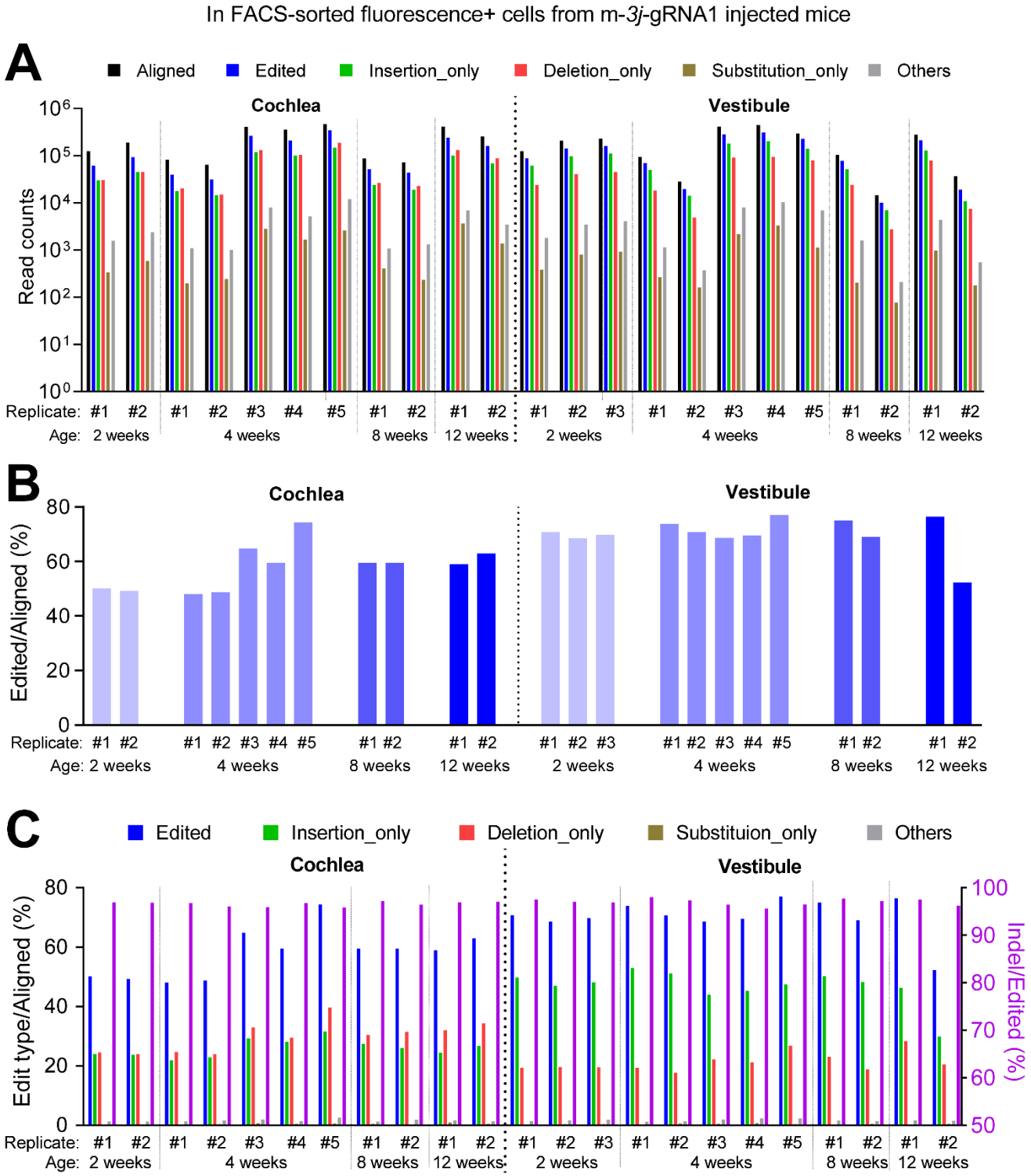

Figure S5. Analysis of editing types in the transfected cochlear and vestibular cells from AAV-m-*3j*-gRNA1 injected mice, related to Figure 4. (A) Number of reads classified by sequence editing types. All samples used in this study are shown per replicate and per time point. (B) Fractions of the edited reads in the total aligned reads from the m-*3j*-gRNA1 transfected cells in the cochleae and the vestibules.

The cochleae and the vestibules were collected from the AAV-m-*3j*-gRNA1 injected *av3j/av3j;Cas9+* mice. The data are shown per replicate and per time point. (C) The percentages of different editing types in the total aligned reads. The insertions and deletions are predominant compositions in the edited reads from the gRNA-treated samples.

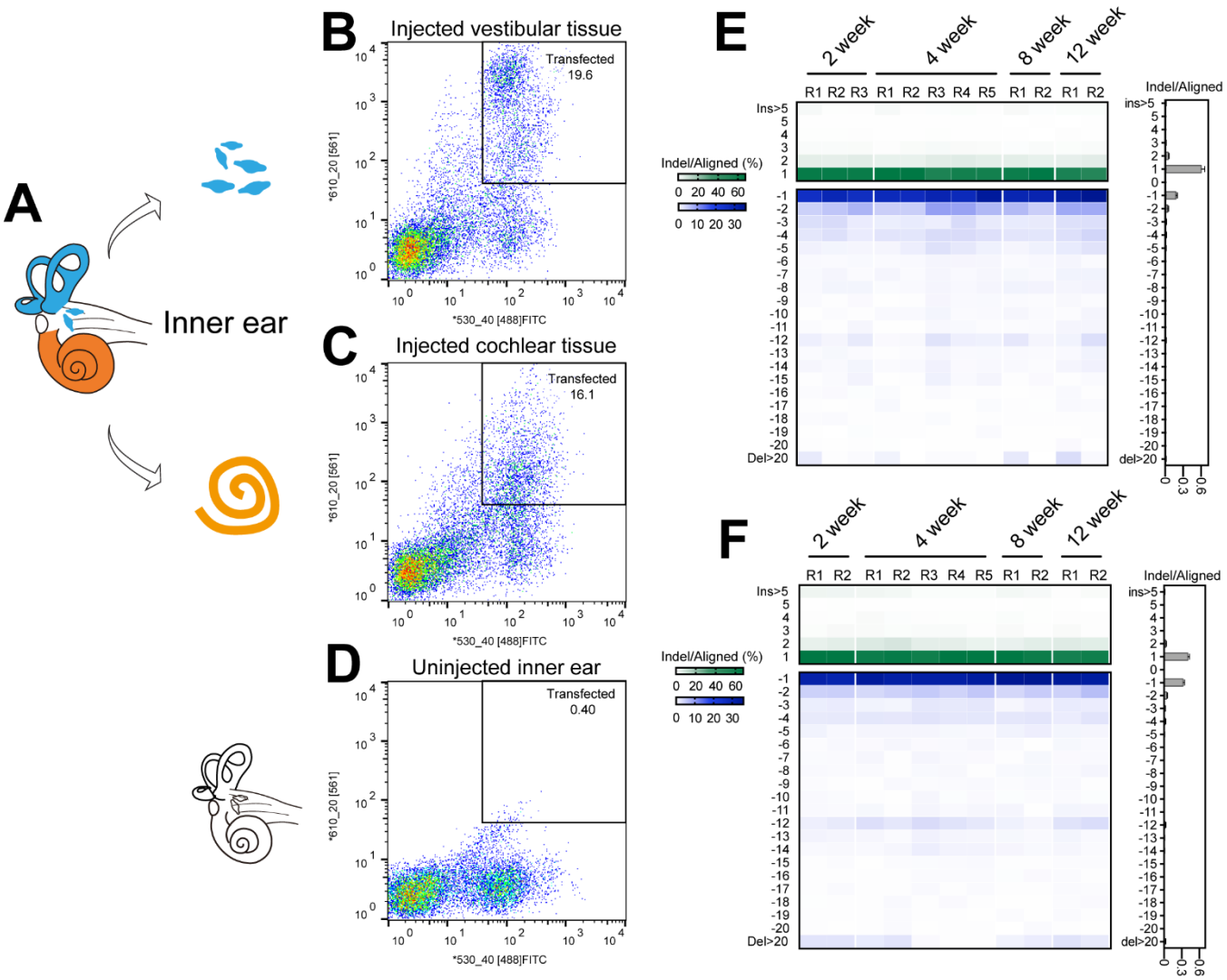

Figure S6. The editing profiles are stable in the AAV-m-*3j*-gRNA1 injected mice when ageing, related to Figure 4. (A) A cartoon illustrating dissociation of cochlear and vestibular tissues prior to FACS collection. (B-D) Raw FACS data of vestibular (B) and cochlear (C) tissues from injected *av3j/av3j;Cas9+* mice (P1 + 12 weeks PVD) and inner ears (D) from uninjected 12-week-old *av3j/av3j;Cas9+* mice. (E and F) Heatmap showing the fraction of each indel in the total aligned reads from the transfected vestibular (E) and cochlear (F) tissues from the injected *av3j/av3j;Cas9+* mice. Tissues were harvested from mice at 2, 4, 8, and 12 weeks after virus injection. The averaged fractions at each indel size are shown on the right. The indel fractions are stable all along the tested time.

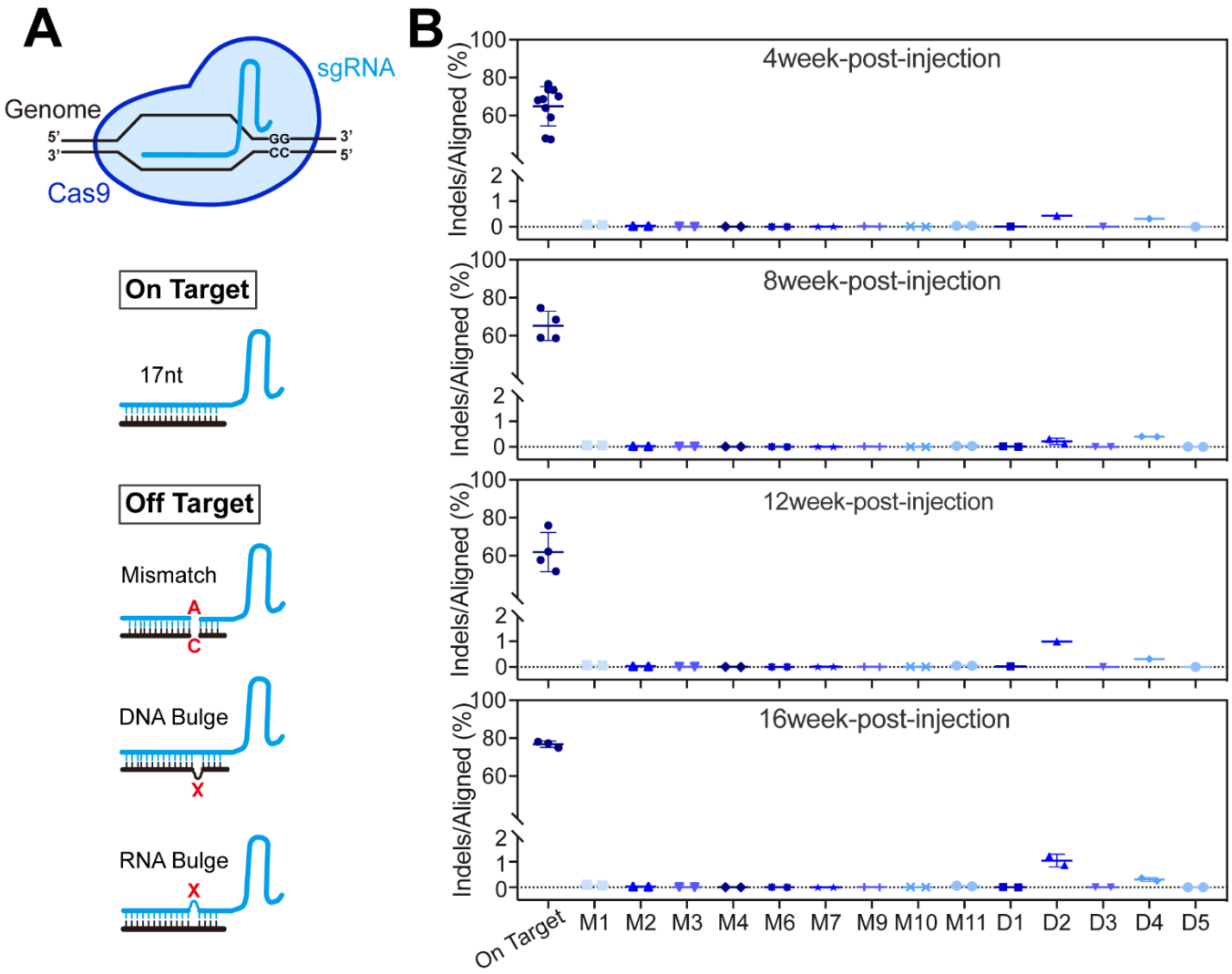

Figure S7. Long-term evaluation of the off-target effects in the AAV-m-*3j*-gRNA1 injected mice, related to Figure 4. (A) A cartoon illustrating how the off-target sites were determined, in which 9 mismatch and 5 DNA bulge sites were selected. No RNA bulge site were chosen, for only 16 bp are available for binding, which is below the minimal length required for a successful cleavage. (B) The indel frequencies in all selected off-target loci in tissues harvested from *av3j/av3j;Cas9+* mice at 4, 8, 12, and 16 weeks PVD. M, mismatch; D, DNA bulge. The mismatch off-targets were predicted by CCtop, and DNA bulge sites were predicted by Cas-OFFinder (for details, see Methods).

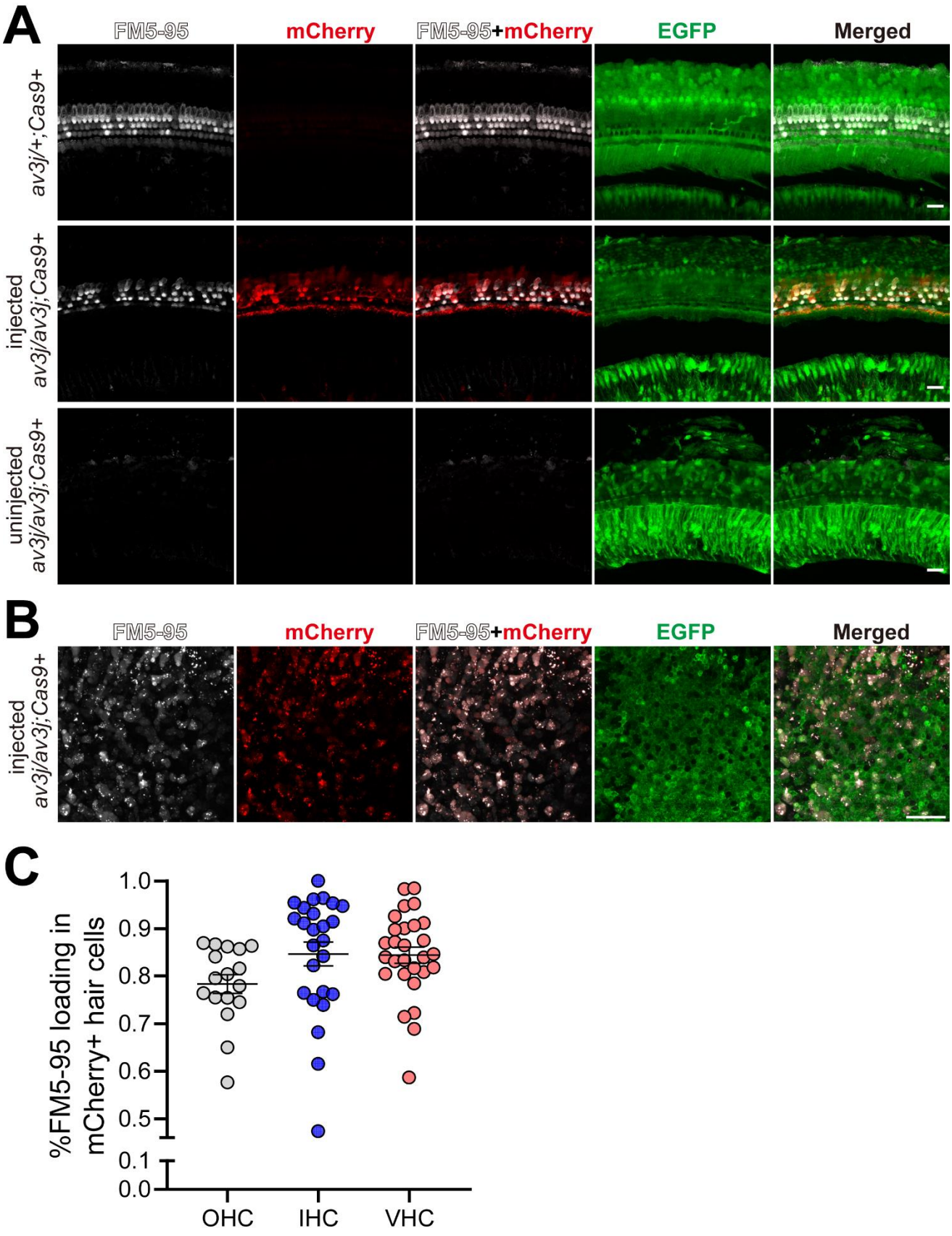
A
FM5-95
mCherry
FM5-95+mCherry
EGFP
Merged
av3j/+;Cas9+
injected av3j/av3j;Cas9+
uninjected av3j/av3j;Cas9+
B
FM5-95
mCherry
FM5-95+mCherry
EGFP
Merged
injected av3j/av3j;Cas9+
C
%FM5-95 loading in mCherry+ hair cells
1.0
0.9
0.8
0.7
0.6
0.5
0.1
0.0
OHC
IHC
VHC

Figure S8. Recovery efficiency of hair-cell mechanotransduction of the AAV-m-*3j*-gRNA1 injected *av3j/av3j;Cas9*+ mice, related to Figure 5. (A) The styryl dye FM5-95, which is permeable to the mechanotransduction channel, was used to evaluate channel activity in hair cells from *av3j/+;Cas9*+, uninjected and injected *av3j/av3j;Cas9*+ mice. Preparations were collected and observed at 7-10 days PVD. After virus delivery, the dye uptake was recovered in *av3j/av3j;Cas9*+ mice, as shown by colocalization of the FM5-95 signals (white) and the virus signals (mCherry, red). The *Cas9* knockin mice also contain EGFP expression cassette, so the green fluorescence was used to indicate the whole cochlea landscape. Some FM5-95 loaded IHCs seem dimmer as they are located in different focal plane. Scale bar, 20μm. (B) FM5-95 uptake in VHCs from injected *av3j/av3j;Cas9*+ mice. Scale bar, 30 μm. (C) Quantification of FM5-95 dye loading in OHCs, IHCs, and VHCs. Each dot indicated a selected view for data quantification (each from 3 mice). Error bars, SEM.

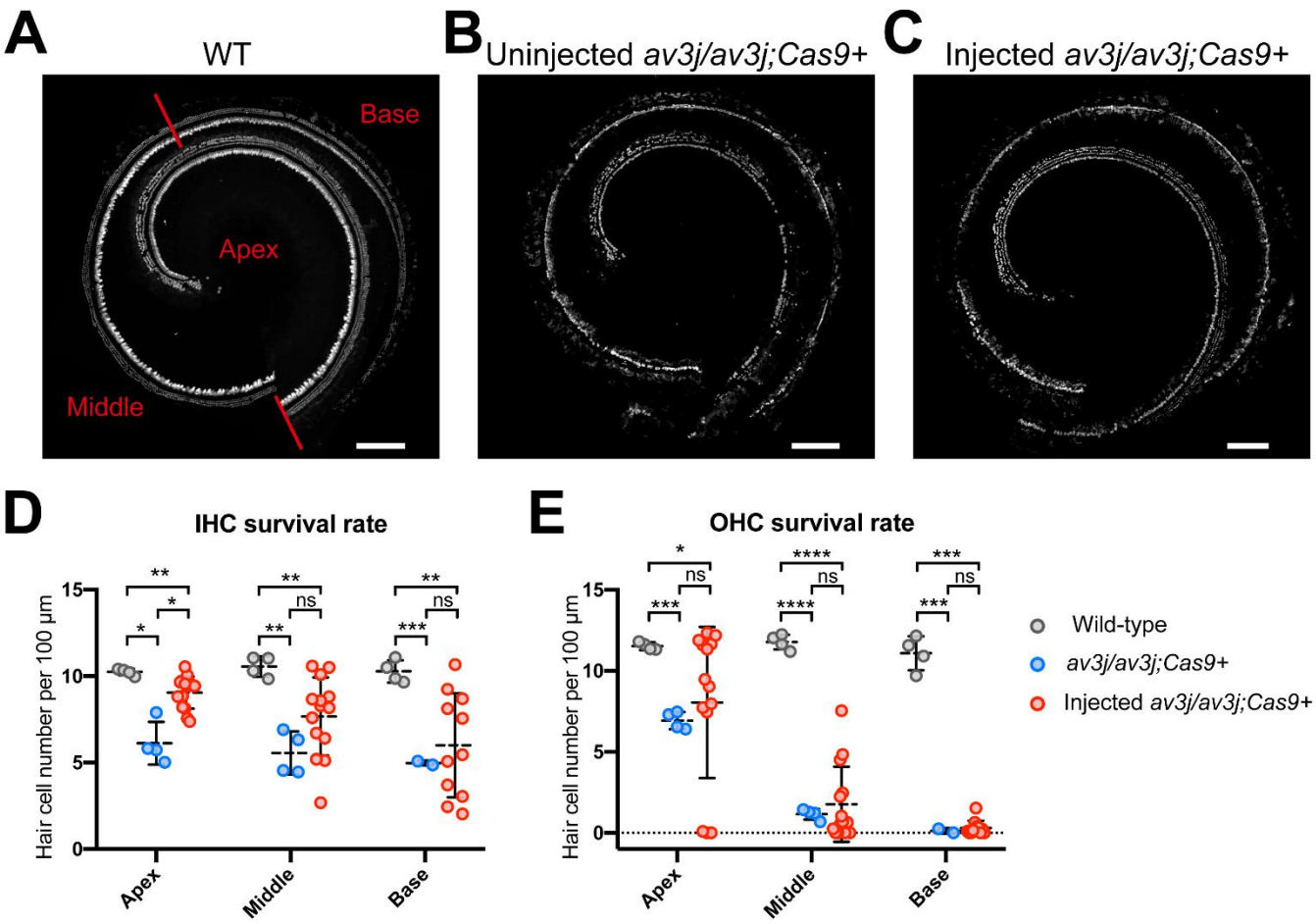

Figure S9. Hair-cell survival analysis of the AAV-m-*3j*-gRNA1 injected *av3j/av3j;Cas9+* mice, related to Figure 5. (A-C) Representative immunostaining images of cochleae from the WT (A), the uninjected *av3j/av3j;Cas9+* (B) and the injected *av3j/av3j;Cas9+* (C) mice at 2 months. The hair cells were labeled by Myosin7a (white). Scale bar, 200 μm. (D and E) Quantification of the survival rate of IHCs (D) and OHCs (E) from the three groups of mice. Each cochlea was separated into 3 segments as shown in (A). Each dot represents one cochlear segment at the position, apex, middle, or base. Comparing to the uninjected control, more IHCs were survived in the injected *av3j/av3j;Cas9+* mice, especially in the apical turn. Brown-Forsythe and Welch ANOVA test; error bars, SEM. ns, no significance, **P* < 0.05, ***P* < 0.01, ****P* < 0.001, *****P* < 0.0001.

Table S1. Raw data of ABR and acoustic startle responses, related to Figures 5.

Injected av3j/av3j;Cas9+ mice with auditory function recovery

No.[a]	Acoustic startle (10^3N/kg)					ABR threshold (dB SPL)								
	90dB	100dB	110dB	120dB	Startle?	Click	4K	5.6K	8K	11.3K	16K	22.6K	32K	ABR?
1[b]	-	-	-	-	-	115	115	115	115	110	115	115	115	Yes
2[b]	-	-	-	-	-	100	115	105	100	95	105	115	115	Yes
3[b]	-	-	-	-	-	100	105	100	95	90	85	90	105	Yes
4	22.50	29.50	30.50	152.50	Yes	100	115	105	100	95	95	95	115	Yes
5	18.60	29.00	150.63	158.71	Yes	100	100	95	90	95	95	110	115	Yes
6	12.40	26.43	54.50	166.67	Yes	105	105	105	105	95	95	95	115	Yes
7	14.40	20.80	34.29	112.75	Yes	95	115	115	100	95	80	90	100	Yes
8	21.50	24.67	123.50	134.67	Yes	105	105	105	100	100	90	85	100	Yes
9	18.67	15.00	33.83	191.00	Yes	95	100	105	100	100	90	115	115	Yes
10	16.00	32.20	35.25	74.00	No	115	115	115	115	115	110	115	115	Yes
11	17.50	17.38	16.17	14.00	No	115	105	100	95	100	105	100	115	Yes
12	12.71	12.14	16.29	8.00	No	105	115	115	105	100	105	115	115	Yes
13	12.13	18.25	66.14	154.86	Yes	95	115	105	95	90	85	95	110	Yes
14	10.88	13.38	61.00	129.50	Yes	90	100	95	85	85	80	105	110	Yes
15	11.88	11.25	61.00	210.75	Yes	105	110	105	95	85	90	90	105	Yes
16	13.00	16.00	116.60	210.17	Yes	100	115	115	115	95	95	100	115	Yes
17	19.20	16.13	40.14	155.83	Yes	105	115	115	100	90	105	100	115	Yes
18[c]	-	-	-	-	-	95	90	90	90	80	85	115	105	Yes
19	10.57	19.63	255.63	303.63	Yes	115	115	105	95	100	100	105	115	Yes
20	13.67	19.00	93.50	199.40	Yes	95	105	105	85	80	95	100	115	Yes
21	10.75	12.00	173.00	369.71	Yes	95	90	90	80	75	75	105	100	Yes
22	16.83	18.29	150.43	244.14	Yes	95	90	95	85	75	75	75	100	Yes
23	20.14	17.71	53.38	190.00	Yes	115	110	115	115	115	115	115	115	Yes
24	12.86	41.67	150.71	298.25	Yes	95	90	95	85	75	80	80	100	Yes
25	11.71	55.00	176.57	214.17	Yes	95	90	90	85	75	80	100	100	Yes
26	13.50	14.50	30.80	207.75	Yes	100	115	105	95	85	95	85	95	Yes
27	15.38	38.17	230.75	340.14	Yes	90	105	100	85	85	85	100	105	Yes
28[c]	-	-	-	-	-	105	105	100	100	90	90	95	105	Yes
29[c]	-	-	-	-	-	105	105	100	95	95	90	115	105	Yes
30	9.80	46.40	162.86	389.71	Yes	75	105	100	90	80	75	90	110	Yes

a. The No. of each animal are ranked by date of birth (DOB) instead of real animal ID, for some mice in different DOB may had the same ID.
b. Startle were not done for the stop of experiment during COVID-19 epdemic.
c. Startle were not done for animal died of treatment-unrelated reasons: unproper anesthesia or care during ABR and fighting.
ABR thresholds ≤ 80 dB SPL were highlight in red.

Acoustic startle responses for WT mice

No.	Acoustic startle (10^3N/kg)			
	90dB	100dB	110dB	120dB
1	23.86	120.88	345.17	707.29
2	28.17	107.71	201.00	362.50
3	16.50	32.14	119.57	150.00
4	26.75	196.00	255.88	665.57
5	19.43	47.00	101.00	416.88
6	17.86	156.67	553.71	650.13
7	15.00	87.33	385.29	482.43
8	25.14	197.86	380.25	897.43
9	44.29	166.75	313.67	487.67
10	50.57	174.71	466.14	445.14

Table S2. Off-target information for av3j mutation, related to STAR Methods.

	Name	Mismatch Number	Sequence	PAM	Chromosome	Strand	Indel%[a]
Mismatch	OT-MM-1	2	CAGCAAGGAAGAAAGCT	TGG	chr17:46148255-46148274	-	0.07089138
	OT-MM-2	2	AATCTAGGAAGAAAGCT	TGG	chr6:30673102-30673121	+	0.03018781
	OT-MM-3	2	AAACCAGGAAGAAAGCT	GGG	chr15:88720061-88720080	+	0.00688479
	OT-MM-4	2	AAGTGGGGAAGAAAGCT	AGG	chr14:117256960-117256979	-	0.00579031
	OT-MM-6	2	AAGAGAAGAAGAAAGCT	TGG	chr1:133738434-133738453	+	0.00334854
	OT-MM-7	3	CAGTAAGGAAGAAAGCT	AGG	chr1:89881732-89881751	+	0.00444832
	OT-MM-9	3	ATGGAAGGAAGAAAGCT	GGG	chr1:66748398-66748417	-	0.01204795
	OT-MM-10	3	AGGGAAGGAAGAAAGCT	GGG	chr17:15936009-15936028	+	0.00871226
DNA bulge	OT-MM-11	3	GAGGGTGGAAGAAAGCT	GGG	chr7:43845453-43845472	+	0.04371001
	OT-DNA-1	1	AAGCcAGGAAGAAGAGCT	GGG	chr7:82072204-82072065	+	0.01256795
	OT-DNA-2	1	AAGCtAGGAAGAGAAGCT	AGG	chr8:41134465-41134486	+	0.65937682
	OT-DNA-3	1	AAGgGAGAGAAGAAAGCT	AGG	chr8:108630756-108630777	-	0.00319279
	OT-DNA-4	1	AAGCcAGGAATGAAAGCT	AGG	chr11:75469158-75469179	+	0.33794297
	OT-DNA-5	1	AtGCTGAGGAAGAAAGCT	GGG	chr1:193440971-193440992	-	0.00217248

a. Average of indel frequency in all samples tested.

Table S3. Primers used for off-target sequencing, related to STAR Methods.

Name	Primer Sequence
Seq OT-DNA-1 F	ACACTCTTTCCCTACACGACGCTCTTCCGATCTGCTCTCAAGTGGCTTGGCTA
Seq OT-DNA-1 R	GACTGGAGTTCAGACGTGTGCTCTTCCGATCTTTCCCCAAATCATCTGAAGG
Seq OT-DNA-2 F	ACACTCTTTCCCTACACGACGCTCTTCCGATCTAGCAGCACTGATTGTTCTCG
Seq OT-DNA-2 R	GACTGGAGTTCAGACGTGTGCTCTTCCGATCTGGACTTTGGCTTTCAAGTGG
Seq OT-DNA-3 F	ACACTCTTTCCCTACACGACGCTCTTCCGATCTAGCATCTGTCTGGCTCCTGT
Seq OT-DNA-3 R	GACTGGAGTTCAGACGTGTGCTCTTCCGATCTAGGAAAAGCAGGGACTGGAT
Seq OT-DNA-4 F	ACACTCTTTCCCTACACGACGCTCTTCCGATCTTGAGTTGGAGGGAGGTTTTG
Seq OT-DNA-4 R	GACTGGAGTTCAGACGTGTGCTCTTCCGATCTTATCTAGGGGGCATGAGCAG
Seq OT-DNA-5 F	ACACTCTTTCCCTACACGACGCTCTTCCGATCTCCTGCACTCTGGGGAATGTA
Seq OT-DNA-5 R	GACTGGAGTTCAGACGTGTGCTCTTCCGATCTGGGATCAAGGCACAGCTAAC
Seq OT-MM-1 F	ACACTCTTTCCCTACACGACGCTCTTCCGATCTTTCCTCACGAAACCCAACAT
Seq OT-MM-1 R	GACTGGAGTTCAGACGTGTGCTCTTCCGATCTAGCCTGCTGACACTTCCTGT
Seq OT-MM-2 F	ACACTCTTTCCCTACACGACGCTCTTCCGATCTTCCTGTCTCCTTCACCGTGT
Seq OT-MM-2 R	GACTGGAGTTCAGACGTGTGCTCTTCCGATCTGAGCCAGGTGGGTCTATGA
Seq OT-MM-3 F	ACACTCTTTCCCTACACGACGCTCTTCCGATCTGATTTCGAACTCCTCCGACA
Seq OT-MM-3 R	GACTGGAGTTCAGACGTGTGCTCTTCCGATCTCTGTCTCTGCCTCCCAAGTG
Seq OT-MM-4 F	ACACTCTTTCCCTACACGACGCTCTTCCGATCTGCAATTGAGATATCAGCACCAA
Seq OT-MM-4 R	GACTGGAGTTCAGACGTGTGCTCTTCCGATCTAGATGGGGGCTTCTTAATCC
Seq OT-MM-5 F	ACACTCTTTCCCTACACGACGCTCTTCCGATCTGAGGGACCAGAGGAAGAAAAA
Seq OT-MM-5 R	GACTGGAGTTCAGACGTGTGCTCTTCCGATCTCATTCCCTGGAGTCCACAGT
Seq OT-MM-6 F	ACACTCTTTCCCTACACGACGCTCTTCCGATCTTGCCATCCTCTCAAACAACA
Seq OT-MM-6 R	GACTGGAGTTCAGACGTGTGCTCTTCCGATCTGGTTGCCCAGGTTTTTATCA
Seq OT-MM-7 F	ACACTCTTTCCCTACACGACGCTCTTCCGATCTACCTGTTCTGCACATTGGTG
Seq OT-MM-7 R	GACTGGAGTTCAGACGTGTGCTCTTCCGATCTAGGAGAGCTCCTGCTGTCAC
Seq OT-MM-9 F2/3	ACACTCTTTCCCTACACGACGCTCTTCCGATCTTGGGAGTATGTGTAGGTAGTCATGG
Seq OT-MM-9 R2	GACTGGAGTTCAGACGTGTGCTCTTCCGATCTCAAACAGGTTCTCTGATGGCATTT
Seq OT-MM-10 F	ACACTCTTTCCCTACACGACGCTCTTCCGATCTGGGCAACATCCTGGAAGATA
Seq OT-MM-10 R	GACTGGAGTTCAGACGTGTGCTCTTCCGATCTCACAGAGAAACCCTGTCTCAAA

Table S4. Sample and experiment counts, related to STAR Methods.

	Panel	Readout	Conditions	Replicate style	Number		
					Cells	Animals (either sex)	Experiments
Figure 1	D	Editing profile	m-3j-gRNA1	2 cochleae/1 mouse		2	2
			m-3j-gRNA2			2	2
			m-3j-gRNA3			2	2
			wm-3j-gRNA4			3	3
Figure 2	C,D,E	Ca imaging of mechanotransduction	av3j/av3j+vector	OHC	15	2	2
			av3j/av3j+m-3j-gRNA1		81	5	5
	E		av3j/av3j+w-3j-gRNA1		17	2	2
			WT+vector		41	3	3
Figure 3	C,D	Ca imaging of mechanotransduction	av3j/av3j+empty	OHC	15	2	2
	C,D		av3j/av3j+WT		23	2	2
	C,D		av3j/av3j+E1373R		23	2	2
	C,D		av3j/av4j+1373delE		27	2	2
	C,D		av3j/av3j+E1373RK		23	2	2
Figure 4	B	Editing profile	2 week cochlea	2 organs/1 mouse		2	2
	B-H		4 week cochlea			5	5
	B		8 week cochlea			2	2
	B		12 week cochlea			2	2
	B		2 week vestibule			3	3
	B-H		4 week vestibule			5	5
	B		8 week vestibule			2	2
	B		12 week vestibule			2	2
	C-H		m-3j-gRNA1			2	2
Figure 5	C	Electrophysiology of mechanotransduction	Control	OHC	19	3	3
			Unjected av3j/av3j;cas9+		9	1	1
			Injected av3j/av3j;cas9+		20	3	3
	D		Control	IHC	18	3	3
			Unjected av3j/av3j;cas9+		11	2	2
			Injected av3j/av3j;cas9+		19	3	3
	F,G	ABR	Control	mouse		12	2
			Injected av3j/av3j;cas9+			52	9
			Unjected av3j/av3j;cas9+			6	1
	H	startle	Control	mouse		10	2
			Injected av3j/av3j;cas9+			24	4
			Unjected av3j/av3j;cas9+			9	2
Figure 6	C	Electrophysiology of mechanotransduction	Control	VHC	12	2	2
			Unjected av3j/av3j;cas9+		16	3	3
			Injected av3j/av3j;cas9+		16	3	3
	E	VOR	Control	mouse		9	2
			Injected av3j/av3j;cas9+			19	6
			Unjected av3j/av3j;cas9+			6	2
	G	Openfield	Control	mouse		4	2
			Injected av3j/av3j;cas9+			21	6
			Unjected av3j/av3j;cas9+			8	3
	H	Rotarod	Control	mouse		5	1
			Injected av3j/av3j;cas9+			21	6
			Unjected av3j/av3j;cas9+			8	3
Figure S1	C-E	Editing profile	m-3j-gRNA1	2 cochleae/1 mouse		2	2
			m-3j-gRNA2			2	2
			m-3j-gRNA3			2	2
			wm-3j-gRNA4			3	3
Figure S2	A-C	Editing profile	m-3j-gRNA1	2 cochleae/1 mouse		2	2
			m-3j-gRNA2			2	2
			m-3j-gRNA3			2	2
			wm-3j-gRNA4			3	3
	A,B		unedited control			3	3
Figure S3		Ca imaging of mechanotransduction	av3j/av3j+vector	IHC	17	5	3
			av3j/av3j+m-3j-gRNA1		16		3
			WT+vector		25	5	5
Figure S4	G	immunostaining	cochlear OHC	tissue organ		3	6
			cochlear IHC				6
			vestibular hair cell			3	5
Figure S5	A-C	Editing profile	2 week cochlea	2 organs/1 mouse		2	2
			4 week cochlea			5	5
			8 week cochlea			2	2
Figure S6	E,F		12 week cochlea			2	2
			2 week vestibule			3	3
			4 week vestibule			5	5
Figure S7	B		8 week vestibule			2	2
			12 week vestibule			2	2
Figure S8	C	immunostaining	cochlear OHC	field view		3	17
			cochlear IHC			3	25
			vestibular hair cell			3	28
Figure S9	D,E	immunostaining	Control	cochlea		2	4
			Unjected av3j/av3j;cas9+			2	4
			Injected av3j/av3j;cas9+			6	11

Movie S1. Injection of DNA into cochlear culture, related to STAR methods.